



Low geomagnetic field intensity in the Matuyama Chron: palaeomagnetic study of a lava sequence from Afar depression, East Africa

Ahn, Hyeon-Seon
Kidane, Tesfaye
Yamamoto, Yuhji
Otofuji, Yo-ichiro

(Citation)

Geophysical Journal International, 204(1):127-146

(Issue Date)

2016-01

(Resource Type)

journal article

(Version)

Version of Record

(Rights)

©The Authors 2015. Published by Oxford University Press on behalf of The Royal Astronomical Society. This article has been accepted for publication in [Geophysical Journal International. 204 (1):127-146, Jan 2016].

(URL)

<https://hdl.handle.net/20.500.14094/90003422>



Low geomagnetic field intensity in the Matuyama Chron: palaeomagnetic study of a lava sequence from Afar depression, East Africa

Hyeon-Seon Ahn,¹ Tesfaye Kidane,² Yuhji Yamamoto³ and Yo-ichiro Otofujii¹

¹Department of Earth and Planetary Sciences, Faculty of Science, Kobe University, Kobe, Japan. E-mail: otofuji@kobe-u.ac.jp

²School of Earth Sciences, College of Natural Science, Addis Ababa University, P.O. Box 1176, Addis Ababa, Ethiopia

³Center for Advanced Marine Core Research, Kochi University, Kochi 783-8502, Japan

Accepted 2015 July 16. Received 2015 July 6; in original form 2015 January 14

SUMMARY

Palaeointensity variation is investigated for an inferred time period spanning from 2.34 to 1.96 Ma. Twenty-nine consecutive lava flows are sampled along cliffs 350 m high generated by normal faulting on the Dobi section of Afar depression, Ethiopia. Magnetostratigraphy and K–Ar measurements indicate a lava sequence of R–N–R–N geomagnetic field polarities in ascending order; the lower normal polarity is identified as the Réunion Subchron. Reliability of palaeomagnetic data is ascertained through careful thermal demagnetization and by the reversal test. The Tsunakawa–Shaw method yielded 70 successful palaeointensity results from 24 lava flows and gave 11 acceptable mean palaeointensities. Reliability in palaeointensity data is ascertained by the similar values obtained by the IZZI–Thellier method and thus 11 reliable mean values are obtained from our combined results. After the older reverse polarity with the field intensity of $19.6 \pm 7.8 \mu\text{T}$, an extremely low palaeointensity period with an average of $6.4 \mu\text{T}$ is shown to occur prior to the Réunion Subchron. During the Réunion Subchron, the dipole field strength is shown to have returned to an average of $19.5 \mu\text{T}$, followed by second extreme low of $3.6 \mu\text{T}$ and rejuvenation with $17.1 \pm 5.3 \mu\text{T}$ in the younger reverse polarity. This ‘W-shape’ palaeointensity variation is characterized by occurrences of two extremely weak fields lower than $8 \mu\text{T}$ prior to and during the Réunion Subchron and a relatively weak time-averaged field of approximately $15 \mu\text{T}$. This feature is also found in sedimentary cores from the Ontong Java Plateau and the north Atlantic, indicative of a possibly global geomagnetic field phenomenon rather than a local effect on Ethiopia. Furthermore, we estimate a weak virtual axial dipole moment of $3.66 (\pm 1.85) \times 10^{22} \text{ Am}^2$ during early stage of the Matuyama Chron (inferred time period of 2.34–1.96 Ma).

Key words: Magnetic field; Magnetostratigraphy; Palaeointensity; Africa.

1 INTRODUCTION

The geomagnetic field is generated from the fluid outer core of the Earth. Its variation through a lengthy period yields information on the hydrothermal dynamic behaviour in the outer core (e.g. Glatzmaier & Robert 1995). Continuous geomagnetic polarity patterns have been inferred from oceanic magnetic anomalies for the last 170 Myr (e.g. Gee & Kent 2009), and continuous records of detailed geomagnetic field variation have been discovered from palaeomagnetic studies of magnetostratigraphy of sedimentary strata from continents, piston core samples of lakes and oceanic basins, and cored samples collected through the Ocean Drilling Program (ODP) and the Integrated Ocean Drilling Program (IODP). The palaeomagnetic records of sediments have established palaeointensity variation since 2–3 Ma (e.g. Sint-2000, Valet *et al.* 2005;

EPAPIA-3 Ma, Yamazaki & Oda 2005; PISO-1500, Channell *et al.* 2009), which has led to the discovery of several geomagnetic excursions (Laj & Channell 2009). Their remanent magnetizations are of depositional remanent magnetization (DRM) and/or post-DRM (pDRM) in their origin, so that these palaeomagnetic records provide skewed geomagnetic field directions (Kodama 2012) and yield only ‘relative’ paleogeomagnetic field intensity (e.g. Tauxe & Yamazaki 2009).

Studying the variation in geomagnetic field intensity further back in time is required for deepening our understanding of behaviour in the outer core. A sequence of lava flows on land is an alternative resource for examining continuous paleogeomagnetic field variation (e.g. Kidane *et al.* 1999; Laj *et al.* 2000, 2011). In addition to preserving the paleogeomagnetic field, lava sequences serve as semi-continuous time series. Their remanent magnetizations

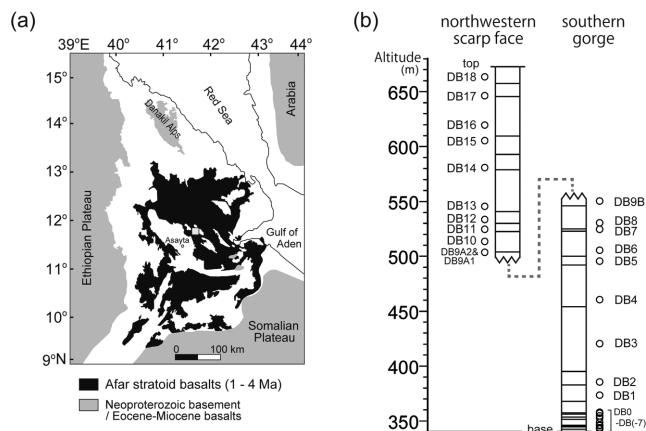


Figure 1. (a) Location map of the Plio–Pleistocene Afar stratoid basalt province and East African triple junction (modified after Beyene & Abdelsalam 2005). Yellow square: location of studied section of lava sequence at the Dobi area. (b) Schematic figure showing vertical positions of the sampled lava flows at the Dobi section. Open circles are sampling positions; solid lines are boundary between lavas.

provide absolute estimations in palaeointensity as well as faithful records in palaeomagnetic direction. Moreover, lavas yield numerical ages from whole rocks and separated minerals when radiometric dating is performed.

Many sequences of lava flows are found in Afar depression which lies at the triple junction of the Red Sea, Gulf of Aden and Ethiopian rifts (Fig. 1a). Recent active tectonics in Afar produced Pliocene–Pleistocene thick sequences of lava flows, which are exposed along high cliffs formed by normal faulting. Such sequences provide an opportunity to investigate continuous geomagnetic field variation by detailed magnetostratigraphic analysis (Carlut *et al.* 1999; Kidane *et al.* 1999). We were able to sample in detail a series of 29 successive lava flows in 2010 along the Dobi cliff, slightly west of the Djibouti–Ethiopian border. We report here the palaeomagnetic directions and absolute palaeointensities from these lava flows as well as radiometric ages determined by K–Ar geochronologic analysis. Because the magnetostratigraphy and palaeointensity record of this lava sequence including the Réunion Subchron was previously reported along the Gamarri cliff ~30 km away from Dobi (Carlut *et al.* 1999; Kidane *et al.* 1999), the geomagnetic field behaviour in the lower Matuyama Chron is discussed here in greater detail.

2 GEOLOGICAL SETTING AND SAMPLING

Afar depression has undergone diffuse tensile deformation. It is bounded by western Ethiopian Plateau to the west, Somalian Plateau to the southeast and the Danakil Alps to the northeast (Fig. 1a). More than 70 per cent of the Afar depression is covered mainly by trap-like basalts known as ‘Afar stratoid basalts’ and some associated rhyolites of Pliocene–Pleistocene age (Valet 1975). These basalts have been dated at 1–3.5 Ma in central Afar by using both K–Ar and ^{40}Ar – ^{39}Ar geochronologies (Courtillot *et al.* 1984; Kidane *et al.* 1999; Lahitte *et al.* 2003).

Good exposures of lava flows of the Afar stratoid basalts occur in a thick sequence along high cliffs formed by normal faulting in the Dobi area (11.84°N, 41.67°E) in central Afar. The study section is a part of the faulted northern edge of the Dobi block (Kidane *et al.* 2003), neighbouring Dobi graben to the northeast.

We sampled 29 lava flows (DB(–7)–DB18) from a section ~350 m long in two parts according to the sampling routes (Fig. 1b). The lower part of the sequence is exposed along an incised erosional gorge toward the south; 18 consecutive lava horizons (DB(–7)–DB9B) were sampled between the basement floor of the entrance to the gorge and the locality in which the inaccessible cliff appears. An additional part of the accessible outcrops above these consecutive lavas occurs in a scarp face near the entrance to the gorge, approximately 1.3 km north of the sampling location of flow DB9B. The upper part of the lava sequence allowed sampling of 11 lava flows (DB9A1–DB18) up to the top of the scarp. Stratigraphic correlation between the two parts was conducted through careful field inspection using a key bed, which was a thin distinct horizon with light reddish-brown colour visible throughout the section. On the basis of field inspection, the lowermost lava (DB9A1) sampled at upper part of the sequence was recognized as a lava flow just above DB9B (Fig. 1b).

It was easy to distinguish each lava flow because four boundaries of DB2/DB3, DB6/DB7, DB11/DB12 and DB12/DB13 were intercalated sediments or paleosols, and the remaining flow boundaries except for DB9A1/DB9A2 are associated with thin baked contacts. Despite the boundary between flows DB9A1 and DB9A2 not being clearly recognized in the field, identification of the two flows was based on palaeomagnetic results, which represented clearly different palaeomagnetic directions. Lava flow thicknesses vary from 1 m to tens of metres with a mean of 14 m.

Four block samples approximately 10–15 cm diameter were collected from each flow with orientation determined by using a magnetic compass. Block samples were also collected from six of the apparently fresh flows for K–Ar age determinations. The present declination value of 1.9° at the sampling sites was evaluated by using the 2010 International Geomagnetic Reference Field (International Association of Geomagnetism and Aeronomy Working Group V-MOD 2010). Locations and altitudes of the sampling sites, in addition to boundaries between lava flows, were determined by using portable Global Positioning System (GPS) equipment. Because all of the flows were observed to be horizontal, no bedding correction was needed.

3 K–Ar DATING

K–Ar dating was performed in the geochronology laboratory at the Research Institute of Natural Science, Okayama University of Science. This analysis was made on plagioclase grains that were separated from the block samples. All samples were aphyric, and no inherited plagioclase xenocrysts were present of under microscopic observation of thin sections.

For appropriate mineral separation, the six samples were crushed by a jaw crusher and a rotary mill and were sieved for 150–200 mesh size fractions. The sieved fractions were washed by distilled water using an ultrasonic bath and were then dried in an oven at 80 °C. After removing magnetic grains by using a hand magnet, the remaining fractions were further sieved and were passed through an isodynamic magnetic separator several times to carefully separate plagioclase grains. To decompose possible associated impurities, the separated plagioclase grains were treated by 3N hydrochloric acid and were rinsed with hot pure water at least 15 times prior to dating.

Concentrations of K in the plagioclase grains were determined by using the flame photometry method (Nagao *et al.* 1984). Low K concentrations were determined by using the low-K analytical method (Itaya *et al.* 1996) with an ultralow blank chemical line.

Table 1. K–Ar age data obtained from the basaltic lava flows for the section (using plagioclase grains).

Sample	Material	K (wt%)	Rad. ⁴⁰ Ar ($\times 10^{-8}$ ccSTP g ⁻¹)	K–Ar age (Ma)	Non-rad. ⁴⁰ Ar (%)
DB18	plagioclase	0.849 \pm 0.017	6.37 \pm 0.19	1.93 \pm 0.07	56.2
DB 8	plagioclase	0.886 \pm 0.018	7.60 \pm 0.19	2.21 \pm 0.07	48.6
DB 6	plagioclase	0.481 \pm 0.010	3.96 \pm 0.14	2.12 \pm 0.09	58.8

Column headings: Sample, sample identification; Material, material analysed; K (wt%), total mean weight percentage of potassium in sample with an experimental error of 2 per cent; Rad.⁴⁰Ar ($\times 10^{-8}$ ccSTP g⁻¹), total amount of radiogenic argon 40 in sample with an experimental error at standard temperature and pressure (0 °C, 1 atm); K–Ar age (Ma), calculated age from duplicated measurements in Ma with an error of 2 σ confidence level; Non-rad.⁴⁰Ar (%), percentage of atmospheric argon 40 per total argon 40 measured in sample.

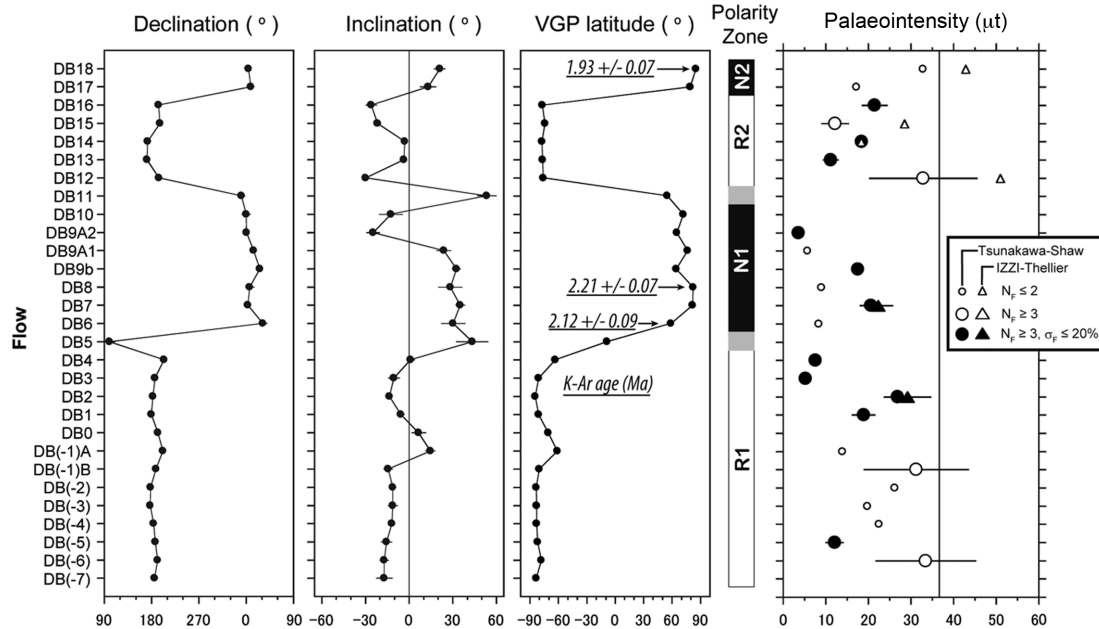


Figure 2. Flow-mean palaeodirection and palaeointensity results of K–Ar aging for 29 individual flows of the lava sequence against the flow code number in stratigraphic order. Declination and inclination: error bars are 95 per cent confidence limit. Polarity zone indicated by black: normal polarity; white: reverse polarity; grey: intermediate polarity. Palaeointensity: error bars are standard deviations; solid symbols represent acceptable data passing the consistency criteria ($N_F \geq 3$ and $\sigma_F \leq 20$ per cent).

The concentration of Ar was analysed by using isotope dilution and the ³⁸Ar spike method (Itaya *et al.* 1991). For this purpose, a 15-cm-radius sector-type mass spectrometer was used. Mass discrimination factors were checked on a daily basis with atmospheric Ar. Specimens wrapped in Al foil were vacuumed at 150–200 °C for approximately 24 h, and Ar extractions were performed at 1500 °C by using an ultrahigh-vacuum line. Reactive gases were removed by using Ti–Zr and Zr–Ar getters. Calculations of ages and errors were carried out using the method described by Itaya *et al.* (1991). In the age calculation, the following decay constants were used: $\lambda_\beta = 0.581 \times 10^{-10} \text{ yr}^{-1}$, $\lambda_e = 4.962 \times 10^{-10} \text{ yr}^{-1}$, $^{40}\text{K}/\text{K} = 1.167 \times 10^{-4}$ (Steiger & Jäger 1977).

K–Ar ages were determined from the three lavas of DB18, DB8 and DB6. The former is located at the top of the section, and the latter two are located at the middle parts of the section, as shown in Table 1 and Fig. 2. The resulting ages, with 2 σ uncertainties, were 1.93 \pm 0.07 Ma for DB18, 2.21 \pm 0.07 Ma for DB8, and 2.12 \pm 0.09 Ma for DB6. The age of flow DB18 is clearly younger than that of the other two. The ages for DB8 and DB6 are indistinguishable at the 2 σ level, giving a weighted mean age of 2.18 \pm 0.06 Ma by the formula of Taylor (1982).

4 ROCK MAGNETISM

Rock magnetic properties were investigated on small chip samples from all 112 sampled blocks at the Center for Advanced Marine Core Research, Kochi University. A magnetic balance (NMB-89, Natsuhara–Giken) was used for thermomagnetic analysis in which the chips were heated up to 700 °C and cooled down to room temperature in a constant field of 0.5 T under a vacuum of 1–10 Pa. Hysteresis parameters of saturation magnetization (M_s), saturation remanent magnetization (M_{rs}), coercive force (B_c) and remanent coercivity (B_{cr}) were determined by conducting hysteresis loop/backfield measurements with a maximum field of 1.8 T using a vibrating sample magnetometer (MicroMag 3900 VSM, Princeton Measurements Corporation).

The resultant thermomagnetic curves indicated that most samples have Curie temperatures (T_c) of 510–580 °C, which suggests the presence of Ti-poor titanomagnetite or pure magnetite (Fig. 3). The curves were classified into the five categories of S, S-, M, M-, and U based on the number of Curie temperature phases and reversibility in the thermomagnetic curves. Reversibility is defined by a net change at a temperature of 100 °C in intensity between heating and cooling processes. The net change of less than 25 per cent is reversible; that

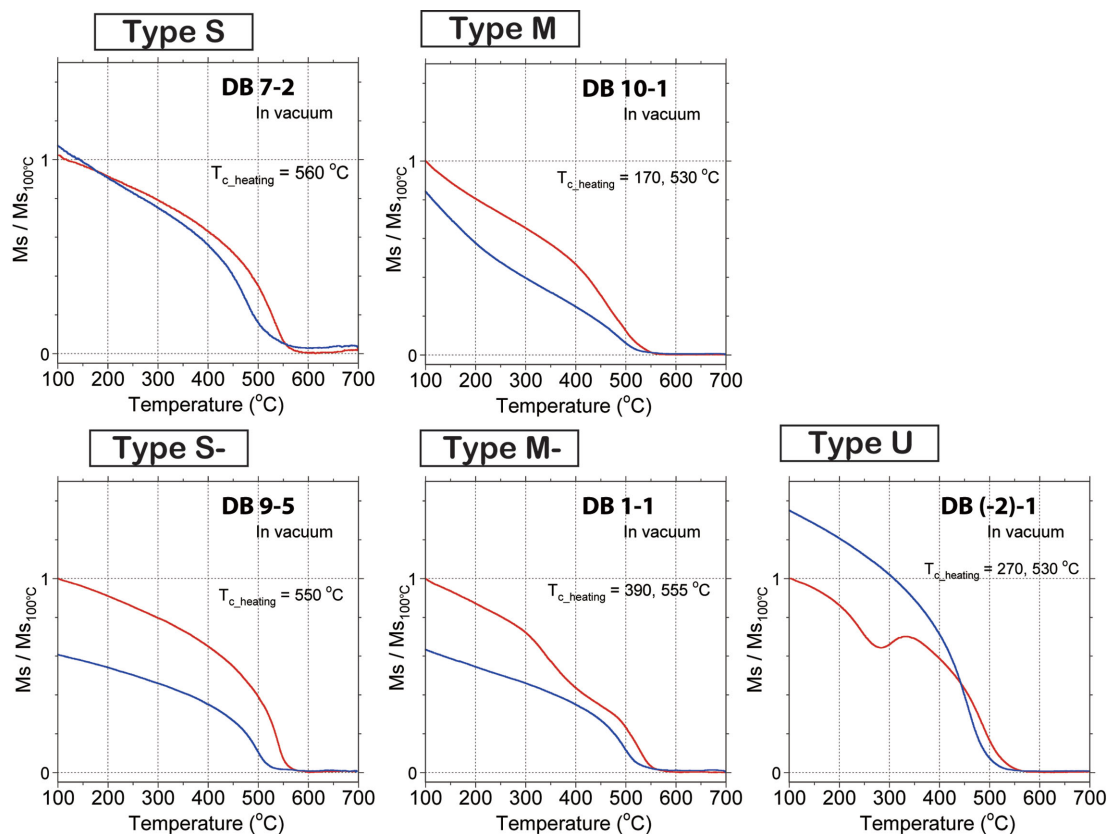


Figure 3. Representative thermomagnetic curves in vacuum runs (1–10 Pa) for the five types including S, S-, M, M-, and U. Variation of saturation magnetization (M_s) normalized by M_s at 100 °C ($M_{s100^\circ\text{C}}$) is shown against temperature. Red (blue) curves indicate heating (cooling) runs.

of more than 25 per cent is irreversible. The five categories are as follows:

Type S (59/112): a single Curie temperature of 510–580 °C; reversible.

Type S- (8/112): a single Curie temperature of 510–580 °C; irreversible.

Type M (3/112): two Curie-temperature phases at ~170–200 °C and ~465–535 °C; reversible.

Type M- (27/112): multiple Curie-temperature phases in heating, but only single phase in cooling; irreversible.

Type U (15/112): a bump shape appears between two Curie-temperature phases; irreversible. This behaviour can be explained by the presence of titanomaghemite, which is inverted to Ti-poor titanomagnetite during heating (e.g. Yamamoto & Tsunakawa 2005; Mochizuki *et al.* 2011).

On the basis of thermomagnetic analysis results, we excluded type U samples from palaeointensity experiments because of thermoremanent magnetization (TRM) replacement by chemical remanent magnetization. Most of the type U samples are recognized in lower part of the section (DB(–7)–DB1).

The ratios of hysteresis parameters M_{rs}/M_s (B_{cr}/B_c) which were calculated after removing paramagnetic contributions, varied from 0.08 to 0.45 (1.4 to 3.3). On a Day plot (Day *et al.* 1977), data from 47 samples plotted within the pseudo-single domain (PSD) region, and those of the other 65 samples plotted much closer to the single domain region (Fig. 4). The distribution of the data points also appeared to be aligned along the theoretical single domain (SD) + multi-domain (MD) mixing curves for magnetite by Dunlop (2002). Thus, the magnetic carriers of the studied

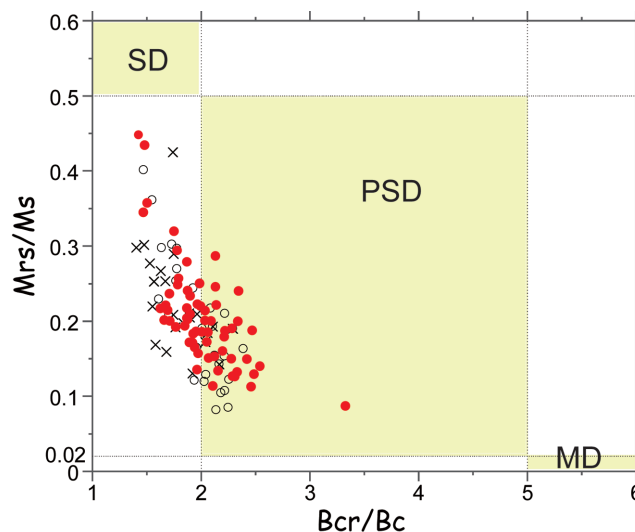


Figure 4. Day plot showing the ratios of hysteresis parameters determined for chip samples from 112 individual blocks, where M_s represents saturation magnetization; M_{rs} : saturation remanence; B_c : coercivity; B_{cr} : coercivity of remanence. Data points are indicated by circles or cross symbols according to whether its neighbouring specimen was used for the palaeointensity experiment. Red solid circles indicate that successful palaeointensity estimates were obtained. All boundary values of individual magnetic domain regions are from those of Dunlop (2002).

samples were interpreted to be PSD or a mixture of SD and MD grains.

5 PALAEOMAGNETISM

5.1 Laboratory procedures

Three or more specimens 25 mm in diameter and 22 mm in height were prepared from each of the collected samples in laboratory. Natural remanent magnetizations (NRMs) were measured with spinner magnetometers at Kobe University (SMM-85, Natsuhara Giken) and at the Center for Advanced Marine Core Research, Kochi University (SMD-88 and Dspin-2, Natsuhara Giken).

Three demagnetization procedures were applied to a total of 282 specimens. One specimen from each of the 112 samples was subjected to stepwise thermal demagnetization (ThD) up to 620 °C by using a thermal demagnetizer (TDE-91C, Natsuhara Giken; residual field less than 5 nT). In addition, two selected specimens from each flow, a total of 58 specimens, were demagnetized by alternating field demagnetizations (AFDs) up to 100 mT using an alternating field (AF) demagnetizer (DEM-8601, Natsuhara Giken). Moreover, a hybrid demagnetization technique was performed on the 112 specimens in which AFDs up to 180 mT followed low-temperature demagnetization (LTD). In this process, the specimens were soaked in liquid nitrogen for 10 min and were then warmed back to room temperature in the zero-field of a Mu-metal shield.

Demagnetization results for each specimen were plotted on an orthogonal vector diagram (Zijderveld 1967) to assess component structures and on an equal-area projection to evaluate directional stability. Principal component analysis (Kirschvink 1980) or the technique of remagnetization circles (Halls 1976, 1978) was used to estimate the directions of different components, whereas site-mean directions were calculated by using Fisherian statistics (Fisher 1953). All the palaeodirectional analysis was performed using the PaleoMac software package by Cogne (2003).

Absolute palaeointensities have been estimated by using the Tsunakawa–Shaw method (e.g. Tsunakawa & Shaw 1994; Yamamoto *et al.* 2003). The IZZI Thellier method (e.g. Tauxe & Staudigel 2004) with partial TRM (pTRM) checks (e.g. Coe *et al.* 1978) was used to cross-check the former palaeointensity results.

The Tsunakawa–Shaw method was applied to 106 specimens from 90 out of 97 block samples pre-selected by thermomagnetic analysis. The remaining 7 block samples were not used because the four directional samples from flow DB11 had no linear primary remanence, and the others were broken during heating. The details of the Tsunakawa–Shaw experiment have been described by Yamamoto & Tsunakawa (2005). In our experiments, for most of the specimens, progressive AFDs were conducted with 2–10 mT steps up to 180 mT, and NRMs, anhysteretic remanent magnetizations (ARMs), and TRMs were measured by using a Dspin-2 automated spinner magnetometer with an AF demagnetizer. For only four specimens, the remanences were measured with an SMD-88 spinner magnetometer and were demagnetized in 17 AF steps up to 140 mT with a DEM-8601C AF demagnetizer. TRMs were imparted in a constant field of 5.00–50.0 µT throughout the heating–cooling cycles up to 610 °C in a vacuum of 5–150 Pa. Hold time at the maximum temperature, 610 °C, was set to 15 (30) min in first (second) heating. Each cooling process took 3 h. In addition, a few grams of activated charcoal were put in the sample tray to limit oxidation of magnetite in every heating process. ARMs were imparted in a 50.0 µT biasing field, which was parallel to the NRM or TRM

directions, with a peak AF of 180 mT. Prior to any progressive AFDs, samples were subjected to LTD.

For palaeointensity determinations, an experimental result for each specimen was plotted on NRM–TRM1* and TRM1–TRM2* diagrams, where TRM1* and TRM2* are the corrected TRMs using the ARM correction technique of Rolph & Shaw (1985) in the first heating and the second heating respectively and expressed as:

$$\text{TRM1}^* = \text{TRM1} \times \text{ARM0}/\text{ARM1}$$

$$\text{TRM2}^* = \text{TRM2} \times \text{ARM1}/\text{ARM2}$$

The slope of the best-fit line on NRM–TRM1* diagram was used for palaeointensity calculation. The TRM1–TRM2* slope was used to check the validity of the ARM correction in which it is expected that the slope is nearly unity if the correction is successful.

The Tsunakawa–Shaw experimental results were judged by the following selection criteria similar to those used by Yamamoto *et al.* (2010):

(1) A primary remanence component of NRM could be isolated by progressive AF demagnetization on the Zijderveld diagram.

(2) On the NRM–TRM1* diagram, a linear portion for the slope calculation should be derived from at least 30 per cent of the extrapolated NRM ($f_N \geq 0.30$, where f is equivalent to that designated by Coe *et al.* 1978) spanned by the chosen segment within the coercivity range of the primary remanence component, and its correlation coefficient is not smaller than 0.995 ($r_N \geq 0.995$). And the highest coercivity of the linear segment is 80 mT or larger.

(3) On the TRM1–TRM2* diagram, a single linear segment also spans not less than 30 per cent of the extrapolated NRM ($f_T \geq 0.30$), and its correlation coefficient is not smaller than 0.995 ($r_T \geq 0.995$). The slope of the chosen segment should be unity within experimental errors ($1.05 \geq \text{slope}_T \geq 0.95$).

Among the remaining samples after the palaeodirectional analyses and the Tsunakawa–Shaw experiments, 55 specimens were selected by the type of the thermomagnetic curve for Thellier-type experiments. The IZZI–Thellier method with pTRM checks was subjected to a series of double heating procedures combined with infield–zero-field (IZ) and zero-field–infield (ZI) temperature steps from room temperature to 600–620 °C in air. An additional temperature step for the pTRM checks was inserted between every other step (ZI step). Each heating–cooling cycle was performed for ~1–1.5 h, including a 20 min hold time at each maximum temperature, by using an electric furnace TDS-1. Remanent magnetizations were measured by using an SMD-88 spinner magnetometer.

The IZZI–Thellier results were also judged by a set of selection criteria similar to those used by Yamamoto *et al.* (2010). Details of the criteria are as follows:

(1) On a vector component diagram, the zero-field data should define a best-fit line with smaller anchored maximum angular deviation (MAD) than 7.0° ($\text{MAD}_{\text{anc}} < 7.0^\circ$), and no significant deviation of the best-fit vector component from the origin should be observed, in which 10° and 10 per cent are adopted as maximum values of θ_{DANG} and dev ($\theta_{\text{DANG}} \leq 10^\circ$ and $\text{dev} \leq 10$ per cent).

(2) On an Arai diagram (Nagata *et al.* 1963), specimens with two clear slopes (or curvature) spanning the blocking temperature interval of the primary remanence were rejected.

(3) At least four data points should be used to estimate the Arai plot linear segment ($N \geq 4$). The correlation coefficient and NRM

fraction of the linear portion used for the interpretation should not be less than 0.990 and 0.300, respectively ($|r| \geq 0.990$ and $f \geq 0.300$).

(4) pTRM checks must have a maximum absolute difference ratio (DRAT) < 7 per cent and CDRAT (defined as the summation of the signed DRAT) < 10 per cent. Definitions of the statistic parameters used above are given in the caption for Table 4.

5.2 Demagnetization results

For the 282 specimens used for palaeodirectional measurements initial NRM intensities ranged from 0.242 A m^{-1} to 47.2 A m^{-1} with a mean of $5.04 \pm 2.79 \text{ A m}^{-1}$. The average intensity for each lava flow is given in Table 2. Fairly large NRM intensities of more than 8 A m^{-1} were observed in the lower and upper flows of the studied section (flows DB(-6), DB(-2), DB2, DB17 and DB18). However, relatively small intensities of less than 2 A m^{-1} were observed in the central part of the section (flows DB3, DB4, DB9A1 and DB9A2) and in flow DB16 in the upper part.

No significant difference in demagnetization behaviour was observed among the ThD, AFD, and hybrid techniques of LTD–AFD (Fig. 5). AFD indicates no soft remanence with strong NRM intensity likely induced from lightning strikes throughout most of the specimens treated. Representative results of ThD are shown in Fig. 6.

In 195 specimens (69 per cent of the total), a small overprinting remanent component was removed by heating to $200\text{--}350^\circ\text{C}$ in ThD and by 20 mT in AFD. Considering the low unblocking temperatures, this component is likely due to recently acquired viscous remanent magnetization (Pullaiah *et al.* 1975). After removal of the overprinting component, a single component magnetization appeared during ThD and AFD (e.g. Fig. 5a). Its unblocking temperature ranged between 530 and 590°C , although complete demagnetization sometimes required higher temperatures up to 620°C for 40 of the 112 specimens (Figs 5a and 6b,d,f,g,h). It is straightforward to determine a characteristic remanent magnetization (ChRM) direction from single component magnetization by principal component analysis (Kirschvink 1980) with a MAD less than $\sim 15^\circ$.

In the orthogonal vector diagram obtained by stepwise ThD or AFD, 77 specimens (27 per cent) yielded in curvilinear trajectories of vector endpoints (e.g. Fig. 5b). The locus of the vector endpoints appeared to lie on a great circle in the equal-area projection (e.g. Fig. 6j). Such demagnetization behaviour suggests overlapping of multiple directional components. Their highest unblocking temperatures were between 530 and 590°C . For 39 specimens, ChRMs were determined by using the remagnetization circle used by Halls (1976, 1978; Fig. 6j), whereas ChRMs of the remaining 38 specimens were barely able to be isolated by the Kirschvink method (1980) above a temperature of $\sim 500^\circ\text{C}$ (Fig. 6c and k).

Erratic demagnetization behaviour such that only a composite vector appeared due to complete overlap of two components, which indicates a meaningless direction, was observed in the remaining 10 specimens. These specimens were precluded from identification of remanent direction.

Mean directions of ChRMs were obtained respectively for three data sets from the distinct demagnetization methods, and resulted in a significant agreement at the 95 per cent confidence levels: $D = 7.0^\circ$ and $I = 15.2^\circ$ ($n = 97$, $k = 15.8$, $a95 = 3.7^\circ$) for ThD; $D = 9.9^\circ$ and $I = 16.2^\circ$ ($n = 66$, $k = 10.3$, $a95 = 5.7^\circ$) for AFD; $D = 10.4^\circ$ and $I = 15.4^\circ$ ($n = 112$, $k = 15.3$, $a95 = 3.5^\circ$) for LTD–AFD. Therefore, we could merge all data into a single data set irrespective

of the methods, and we calculated a mean direction for each lava based on the data set (Table 2). The number of specimens used for the calculation ranged from 5 to 13 for each lava. The calculated within-flow precision parameter was generally high throughout all 29 lava flows ($20.6 < k < 724.8$).

5.3 Directional behaviour

The palaeomagnetic results are listed in Table 2. In Fig. 2, flow-mean inclinations, declinations and their corresponding virtual geomagnetic poles (VGPs) are plotted in stratigraphic order as a function of flow number. A well-defined R–N–R–N polarity sequence was identified from the bottom to top of the Dobi section. The lower part of the section (flows DB(-7)–DB4) has a reversed polarity (R1), the middle part (flows DB6–DB10) shows a normal polarity (N1), a reverse polarity (R2) again appears in the upper part (flows DB12–DB16), and the uppermost two flows of DB17 and DB18 have a normal polarity (N2). This polarity sequence also includes four complete polarity magnetozones in which the VGP latitudes range from 58.7°N to 85.2°N in the normal polarities and from 61.3°S to 84.4°S in the reversed polarities.

Fig. 7 displays the flow-mean palaeomagnetic directions on an equal area projection. Anomalous mean directions were observed from flows DB5 and DB11 (Fig. 7a), resulting in low VGP latitudes with 8.9°S and 55.0°N , respectively (Table 2). These flows are located on the boundary between the R1 and N1 polarity intervals and between the N1 and R2 polarity intervals, respectively. According to the method of Vandamme (1994), which is used to limit the domain of transitional geomagnetic poles, VGP locations of flows DB5 and DB11 were interpreted as transitional during polarity reversals.

Excluding for the two possible transitional data from flows DB5 and DB11, the mean palaeomagnetic directions are $D = 10.4^\circ$ and $I = 17.0^\circ$ ($k = 12.2$, $a95 = 15.4^\circ$, $N = 9$) for the normal polarity sequences and $D = 186.8^\circ$ and $I = -10.7^\circ$ ($k = 32.7$, $a95 = 6.1^\circ$, $N = 18$) for the reversed polarity sequences (Fig. 7a). The two mean directions showed a positive reversal test (McFadden & McElhinny 1990) with classification ‘C’ because the angular distance (γ) obtained by the test was 7.3° which is less than the critical angle of $\gamma_c = 13.2^\circ$.

5.4 Palaeointensity results

The Tsunakawa–Shaw method yielded 70 successful results after application of the selection criteria, showing a high success rate of 66 per cent (Table 3). The successful specimens had moderately large decreases in the first ARM acquired (ARM0) with the LTD procedure with an average demagnetized fraction of 24.7 ± 9.3 per cent. This result indicates a relatively large contribution of MD-like components (e.g. Ozima *et al.* 1964; Heider *et al.* 1992). As shown in Figs 8(a) and (b) for the representative successful results, approximately 70 per cent of such results had linear portions larger than 0.5 of the total extrapolated NRM ($f_N > 0.5$) in the NRM–TRM1* diagrams. The average slope in the ARM0–ARM1 diagrams (Slope_{A1}) was 0.830 ± 0.291 , which indicates that the alteration during laboratory heating was not severe in general. However, some specimens had ARM0–ARM1 slopes that are greatly different from unity such as a Slope_{A1} of 0.303 in DB(-1)-1-B, indicating some heavy thermal alteration. In these cases, the ARM correction worked well and their validity was examined by the double heating test as the slope on the TRM1–TRM2* diagram after the ARM correction was close to

Table 2. Statistical results of palaeomagnetic directions and palaeointensities from basaltic lava flows in the Dobi area of central Afar.

Site locality			Palaeodirection						VGP		Tsunakawa-Shaw palaeointensity			IZZI-Thellier palaeointensity			Combined palaeointensity							
Flow name	Lat (°N)	Lon (°E)	K-Ar age (Ma)	TM Curve	NRM (A m ⁻¹)	N _d	Dec (°)	Inc (°)	α ₉₅ (°)	k	Plat (°)	Plon (°)	N _F	F (μT)	σ _F (%)	N _F	F (μT)	σ _F (%)	N _F	F (μT)	σ _F (%)	VDM (10 ²² Am ²)	VADM (10 ²² Am ²)	
DB18	11.8446	41.6656	1.93 ± 0.07	S	9.53	10/10	4.8	21.0	3.8	161.2	85.2	142.9	2/2	32.8	—	1/2	42.8	—	3/4	36.1 ± 14.5	40.1	—	—	—
DB17	11.8447	41.6658		S	13.6	8/9	9.3	13.1	5.4	105.0	79.4	160.4	2/3	17.2	—	0/2	—	—	2/5	17.2	—	—	—	—
DB16	11.8448	41.6662		S	1.92	10/10	193.1	-26.0	3.8	162.5	-71.1	222.8	4/4	21.5 ± 2.9	13.5	0/3	—	—	4/7	21.5 ± 2.9	13.5	5.14	5.24	—
DB15	11.8448	41.6664		S	6.05	13/13	196.1	-21.6	2.2	345.3	-74.2	312.4	4/7	12.2 ± 3.1	25.4	1/4	28.5	—	5/11	15.4 ± 7.8	50.5	—	—	—
DB14	11.8451	41.6667		S	5.46	10/10	172.6	-3.0	2.1	528.8	-77.3	77.6	4/4	18.5 ± 0.5	2.7	2/4	18.3	—	6/8	18.4 ± 1.4	7.6	4.76	4.49	—
DB13	11.8454	41.6672		S	2.55	10/10	171.2	-3.5	1.9	639.7	-76.7	83.2	4/4	11.2 ± 1.7	15.2	0/4	—	—	4/8	11.2 ± 1.7	15.2	2.89	2.73	—
DB12	11.8454	41.6672		S	5.53	10/10	194.0	-30.0	2.5	364.4	-75.8	292.7	4/4	32.9 ± 12.6	38.3	2/3	51.0	—	6/7	38.9 ± 13.6	34.9	—	—	—
DB11	11.8458	41.6672		S	2.91	9/10	351.3	53.5	6.5	62.9	55.0	347.4	—	—	—	0/1	—	—	0/1	—	—	—	—	—
DB10	11.8458	41.6672		S, M	3.75	8/10	359.9	-12.6	8.0	48.8	71.8	222.0	0/4	—	—	0/1	—	—	0/5	—	—	—	—	—
DB9A2	11.8458	41.6675		S, S-	1.57	5/6	0.8	-24.7	4.4	278.4	65.2	219.8	3/3	3.63 ± 0.46	12.7	0/1	—	—	3/4	3.63 ± 0.46	12.7	0.875	0.884	—
DB9A1	11.8458	41.6675		S	1.88	8/8	13.9	23.9	4.8	134.8	76.4	127.5	1/4	5.74	—	0/2	—	—	1/6	5.74	—	—	—	—
DB9B	11.8352	41.6720		S, M-	3.91	13/13	25.8	32.5	2.8	221.3	64.4	115.4	3/7	17.6 ± 1.2	6.8	0/4	—	—	3/11	17.6 ± 1.2	6.8	4.03	4.29	—
DB8	11.8356	41.6718	2.21 ± 0.07	S, M-	5.04	9/10	6.9	28.3	8.2	40.7	82.6	105.2	2/4	8.98	—	0/2	—	—	2/6	8.98	—	—	—	—
DB7	11.8356	41.6718		S	4.56	9/10	3.3	35.1	3.1	277.0	81.8	64.1	4/4	20.6 ± 2.5	12.1	3/4	22.3 ± 3.3	14.8	7/8	21.3 ± 2.7	12.9	4.78	5.19	—
DB6	11.8358	41.6716	2.12 ± 0.09	S	3.26	9/11	32.0	30.3	8.1	41.8	58.7	119.7	1/5	8.35	—	0/4	—	—	1/9	8.35	—	—	—	—
DB5	11.8358	41.6716		M-, U	4.25	10/11	99.8	43.5	10.9	20.6	-8.9	64.3	0/3	—	—	0/3	—	—	0/3	—	—	—	—	—
DB4	11.8367	41.6711		M-	1.69	11/11	203.8	1.1	2.7	292.4	-63.3	337.7	4/5	7.61 ± 0.36	4.7	0/1	—	—	4/6	7.61 ± 0.36	4.7	1.97	1.85	—
DB3	11.8367	41.6711		S-	1.65	11/11	186.5	-10.4	3.8	142.5	-80.8	356.9	3/5	5.26 ± 0.98	18.6	0/3	—	—	3/8	5.26 ± 0.98	18.6	1.34	1.28	—
DB2	11.8432	41.6689		S	8.99	12/12	182.5	-13.5	1.9	511.9	-84.4	15.2	6/6	26.9 ± 3.0	11.2	3/4	29.2 ± 5.4	18.5	9/10	27.7 ± 3.8	13.6	7.00	6.74	—
DB1	11.8432	41.6689		S, M-, U	3.75	10/10	179.4	-5.6	2.4	400.5	-80.9	45.5	4/4	18.9 ± 2.6	13.8	0/1	—	—	4/5	18.9 ± 2.6	13.8	4.87	4.61	—
DB0	11.8454	41.6700		M-, U	4.54	8/8	192.1	6.6	4.8	131.6	-70.6	2.5	0/2	—	—	0/1	—	—	0/3	—	—	—	—	—
DB(-1)A	11.8454	41.6700		S, S-	4.07	10/10	201.4	14.6	3.4	206.2	-61.3	352.8	1/4	13.9	—	0/3	—	—	1/7	13.9	—	—	—	—
DB(-1)B	11.8454	41.6700		S, M-, U	4.89	9/9	188.5	-14.3	2.9	308.2	-80.4	339.6	3/3	31.3 ± 12.2	39.0	0/1	—	—	3/4	31.3 ± 12.2	39.0	—	—	—
DB(-2)	11.8454	41.6700		M-, U	8.20	8/8	178.0	-11.1	2.1	724.8	-83.5	59.4	1/1	26.2	—	—	—	—	1/1	26.2	—	—	—	—
DB(-3)	11.8454	41.6700		M-, U	4.00	8/8	177.4	-11.1	3.2	292.2	-83.2	64.3	2/2	19.8	—	—	—	—	2/2	19.8	—	—	—	—
DB(-4)	11.8454	41.6700		M-	5.66	11/11	183.9	-11.8	2.1	485.7	-83.0	8.1	2/4	22.5	—	—	—	—	2/4	22.5	—	—	—	—
DB(-5)	11.8454	41.6700		S, S-	7.16	10/10	187.1	-15.4	3.7	170.1	-81.9	340.8	3/3	12.1 ± 2.0	16.5	—	—	—	3/3	12.1 ± 2.0	16.5	3.05	2.95	—
DB(-6)	11.8454	41.6700		M-, U	9.05	10/10	191.6	-17.1	2.9	278.4	-78.2	325.8	3/4	33.5 ± 11.7	34.9	—	—	—	3/4	33.5 ± 11.7	34.9	—	—	—
DB(-7)	11.8454	41.6700		S, U	6.24	6/7	186.0	-17.0	5.4	154.5	-83.3	339.2	0/1	—	—	—	—	—	0/1	—	—	—	—	—

Column headings: Flow name, flow code number recognized; Lat (°N) and Long (°E), latitude and longitude of each sampling location; TM curve, types of thermomagnetic curve observed; NRM (A m⁻¹), average intensity of initial natural remanent magnetization (NRM); N_d, number of specimens used for calculating the mean direction/number of specimens measured for palaeomagnetic analysis; Dec (°), Inc (°), α₉₅ (°), and k, characteristic mean direction, 95 per cent confidence limit of circle, and precision parameter; Plat (°N) and Plon (°E), latitude and longitude of the resulting virtual geomagnetic pole (VGP); N_F, number of specimens used to calculate mean palaeointensity per flow/number of specimens subjected to palaeointensity measurement; F (μT), mean value of palaeointensity with its standard deviation; σ_F (%), ratio of the standard deviation to the mean palaeointensity; V[A]DM (10²² Am²), acceptable average virtual [axial] dipole moment for the combined palaeointensity data.

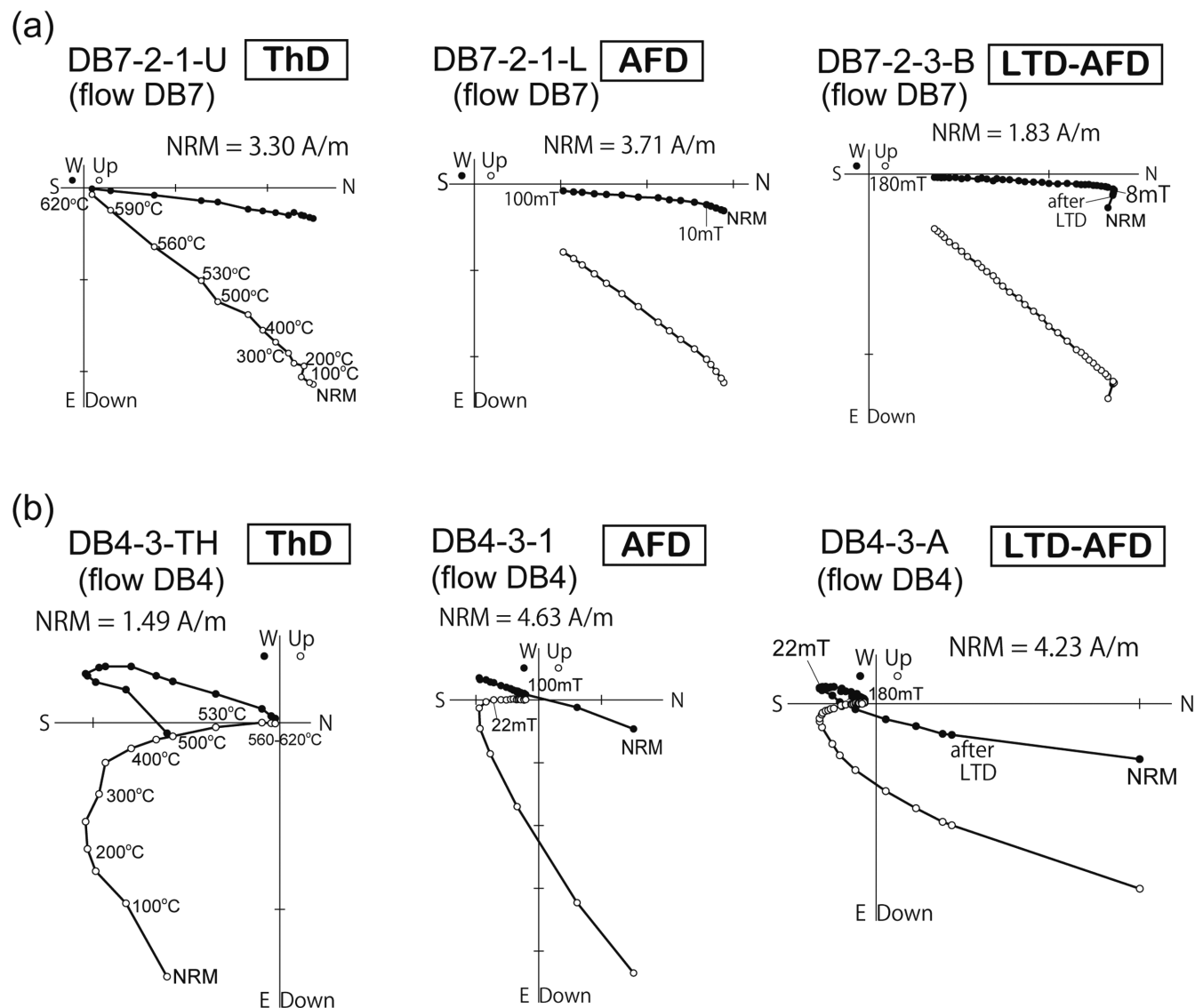


Figure 5. Comparison of the demagnetization behaviours for two block samples (DB7-2 and DB4-3) with respect to the three different procedures of thermal demagnetization (temperature in °C), alternating field (AF), and low-temperature demagnetization (LTD)–AF demagnetization (AFD; field in mT). Orthogonal vector diagrams (Zijderveld 1967) are shown in geographic coordinates. Open (solid) circles represent the component in the vertical (horizontal) plane.

unity. Unsuccessful results, such as those shown in Fig. 8(c), were rejected mainly due to low values of the correlation coefficients in the NRM–TRM1* diagrams ($r_N < 0.995$) and non-unity slopes in the TRM1–TRM2* diagrams ($\text{Slope}_T < 0.95$ and $1.05 < \text{Slope}_T$).

The IZZI–Thellier experiments gave only 12 successful results for a success rate of 22 per cent. Examples of Arai diagrams and orthogonal vector projection plots of the zero-field steps are shown in Fig. 9. Specimen DB7–2–3-A exhibited reasonably good behaviour such that almost all data points tended to lie on a single straight line ($r = 0.994$) with positive pTRM checks (Fig. 9a). After removal of a small fraction of the low blocking temperature range up to 300–450 °C, the majority of remaining successful specimens showed a single slope in the Arai diagram (Fig. 9b). The low blocking temperature segment can be considered as obvious contamination by VRM in the orthogonal vector diagram. All 12 successful results provided linear segments from more than 65 per cent of the total extrapolated NRM ($f > 0.65$) with at least 8 data points in the NRM–TRM diagram. These linear segments were also determined by

blocking temperature intervals including 450–600 °C. In contrast, NRM–TRM diagrams from 43 specimens that failed selection had only small linear segments and low correlation coefficients. For example, Fig. 9(c) illustrates a representative rejected result in which the Arai diagram is concave-up and the pTRM checks failed above 520 °C. This characteristic was found in 28 rejected specimens.

For 11 samples both of two palaeointensity estimates were obtained from both the IZZI and Tsunakawa–Shaw methods. This includes two results from the Tsunakawa–Shaw method for samples DB2–1 and DB2–2, which both yielded only one IZZI method result. The two data sets allow a comparison of the results from the two methods when each set of the tied data is simply averaged (Fig. 10). Both methods yield comparable results, with exception of DB2–1 and DB12–4, which have a ratio of the Thellier-type estimate to the Shaw-type estimate as high as ~ 1.2 (Fig. 10a). Additionally, the palaeointensity data sets were also compared using the Wilcoxon rank-sum test, which is a non-parametric test (Fig. 10b). Median values in the Tsunakawa–Shaw and IZZI–Thellier data sets were

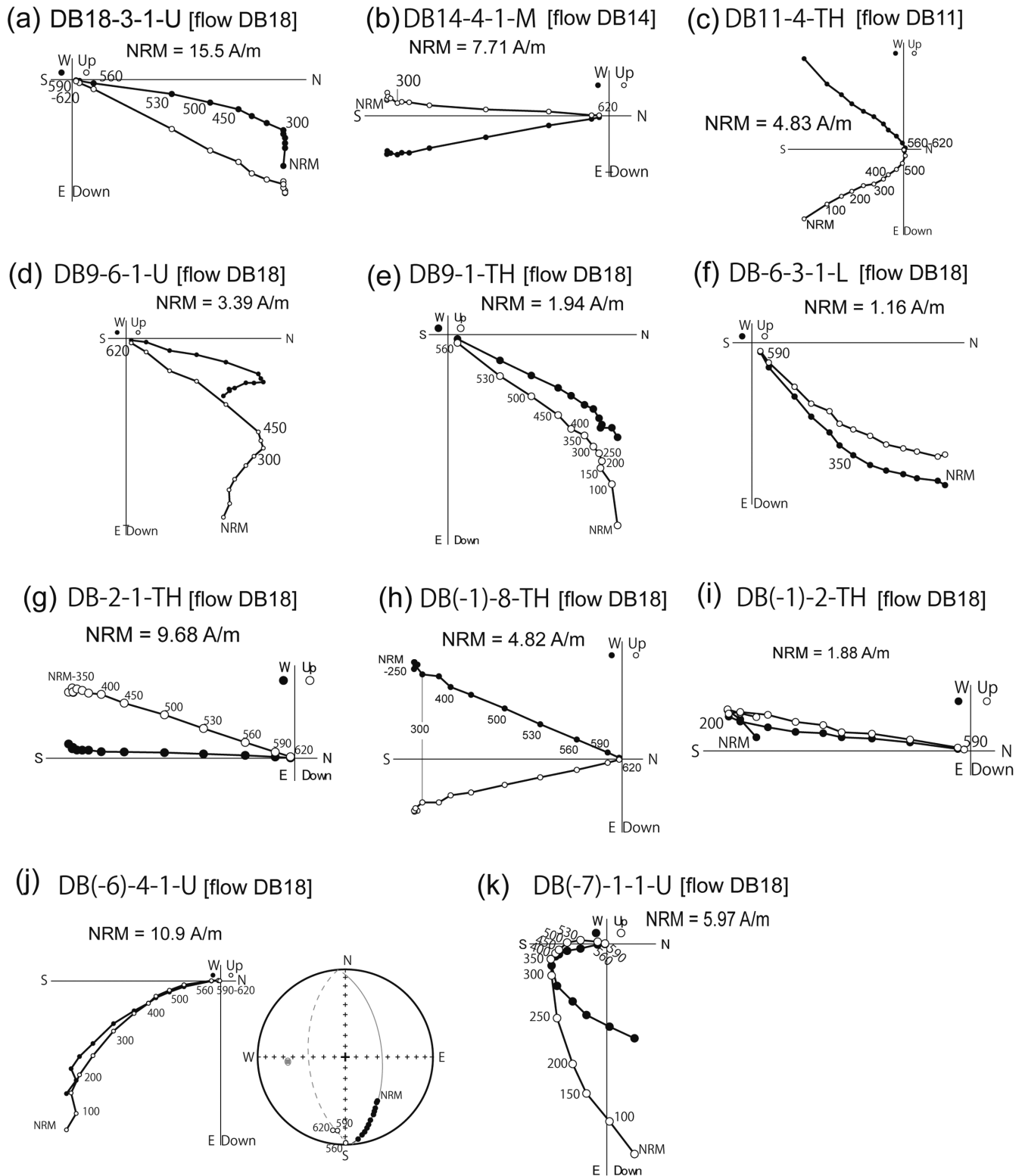


Figure 6. Thermal demagnetization diagrams of representative specimens. Orthogonal vector diagrams (Zijderveld 1967) are shown in geographic coordinates. Open (solid) circles represent the component in the vertical (horizontal) plane. Equal area projection of the demagnetization results are also shown in (j), showing that the data lie close to a common great circle (grey line and square symbol as a normal vector perpendicular to the plane of the great circle fitting). Characteristic remanent magnetization (ChRM) directions were determined by best-fit straight line for (a) and (b), (d)–(i) and (k) and barely (c), whereas (j) yielded ChRM direction using only a remagnetization circle.

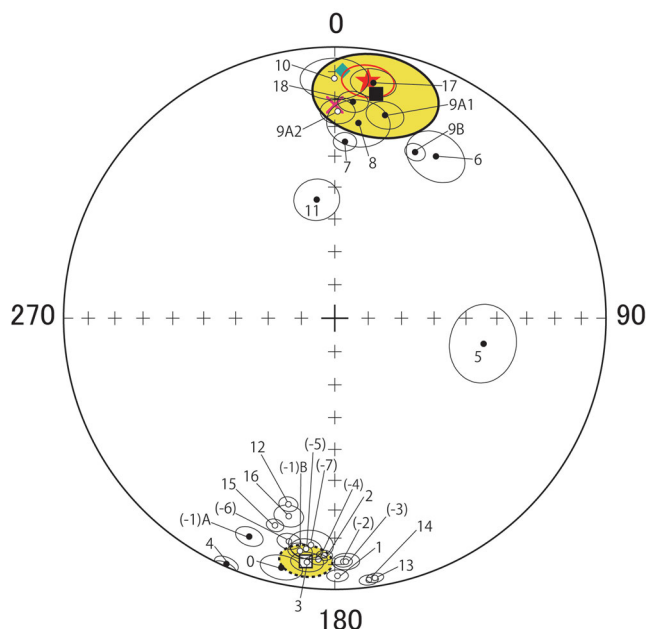


Figure 7. Equal-area projection of flow-mean characteristic remanent magnetization (ChRM) directions for all 29 lavas from the section. Solid (open) symbols indicate downward (upward) inclinations. The pink cross (green diamond) symbol denotes the geocentric axial dipole (present International Geomagnetic Reference Field; IGRF) direction at the location. An oval around each mean direction represents 95 per cent confidence limit (α_{95}). Overall means for the reversed and normal direction data are shown as square symbols with 95 per cent confidence limits (yellow filled ovals). In the calculation of overall means, two transitional data sets from flows DB5 and DB11 were discarded. The red star represents the overall mean for the 27 flows with a 95 per cent confidence limit.

26.6 μT and 25.5 μT , respectively. The result of the test indicates that the distributions of the two data sets have no statistically significant difference (Mann–Whitney $U = 53.0$, $n_T = n_S = 11$, $P = 0.646$ two-tailed). Therefore, it maintains that our palaeointensity estimates not vary with the methods and can be unambiguously determined.

The success rates of the Tsunakawa–Shaw and IZZI–Thellier methods differed significantly; the former was three times higher than the latter. This result is likely attributed the effect of MD remanence carriers to TRM in our samples. Whereas the present Tsunakawa–Shaw experiments have likely removed of this contribution by LTD treatment, the IZZI–Thellier ones have not. An additional possibility is the difference in atmosphere. The Tsunakawa–Shaw experiments used a vacuum, whereas the IZZI–Thellier experiments used air.

5.5 Mean palaeointensities for lava flows

Of 29 lava flows, 24 yielded flow-mean palaeointensities by using the Tsunakawa–Shaw method. Fifteen lava flows consisted of more than three palaeointensity results, whereas other lava flows consisted of less than three data sets including one and two data sets from four and five flows, respectively. The flow-mean palaeointensities were calculated in Table 2 and plotted in Fig. 2.

We followed the set of criteria used by Yamamoto *et al.* (2007) for acceptance of the flow-mean and they required at least three specimen-level palaeointensities per flow with a maximum standard deviation of 20 per cent of the mean. A total of 11 flow-mean

palaeointensities pass these criteria, as shown by solid circles in Fig. 2. The acceptable flow-means varied between 3.63 μT and 26.9 μT , and their grand mean for the lava sequence was 14.9 μT with a standard deviation of 7.4 μT . This value is 40 per cent of the present geomagnetic field intensity of $\sim 37 \mu\text{T}$ at central Afar (International Association of Geomagnetism and Aeronomy Working Group V-MOD 2010). Thus, low palaeointensity characterizes the paleogeomagnetic nature of the Dobi area. It is notable that all the reliable flow-mean palaeointensities were obtained from flows with a stable polarity direction.

A noticeable characteristic of palaeointensity variation for the lava sequence is the occurrence of two particularly low field intervals. The lower interval consists of two lava flows, DB3 and DB4, which correspond to the late stage of the R1 polarity interval preceding the N1 interval. The upper interval was formed by one lava flow, DB9A2, which corresponds to intra-N1 polarity interval (Fig. 2; Fig. 11a). The palaeointensities of these fields were lower than 8 μT . Furthermore, a relatively high field intensity interval was noted between the two low-field intervals in which the palaeointensity increased up to 20.6 μT . This somewhat high-field feature occurred in the N1 polarity interval.

The IZZI–Thellier method yielded flow-mean palaeointensities from seven lava flows although only two flows, DB2 and DB7, fulfilled the reliability criteria for acceptance of a flow mean. Their individual means were 29.2 μT for DB2 and 22.3 μT for DB7, which are comparable to those estimated from the Tsunakawa–Shaw method (Table 2; Fig. 2).

The concordance between the two sets of palaeointensity results allowed all the palaeointensity results from both methods to merge into a single data set, which ensures that the overall results are not biased by a single method and should surely yield more robust results. Flow-mean palaeointensities were recalculated from the combined data set and their values were reported in Table 2. As in the case of the Tsunakawa–Shaw results, the combined palaeointensity results yielded 11 reliable flow means passing the flow-mean acceptance requirements. The values ranged from 3.63 μT to 27.7 μT and their overall mean is 15.0 μT with a standard deviation of 7.6 μT , which is near identical to the Tsunakawa–Shaw results. Further considerations will discuss the paleo-field intensity and its variation combined with our new results.

6 DISCUSSION

6.1. Magnetostratigraphy

The palaeomagnetic directions obtained from the lava flows in the Dobi section reveal a clear record of geomagnetic polarity change (Fig. 2). A stable reverse (R1) polarity magnetozone is observed in the lower part of the lava sequence, followed by stable normal (N1), reverse (R2) and normal (N2) polarity magnetozones. The lower normal-polarity (N1) magnetozones have been dated at $2.21 \pm 0.07 \text{ Ma}$ (DB8) and $2.12 \pm 0.09 \text{ Ma}$ (DB6), whereas the age of the upper normal-polarity (N2) magnetozones is $1.93 \pm 0.07 \text{ Ma}$ (DB18). A comparison of the observed ages and polarity sequence with the latest geomagnetic polarity time scale (GPTS) expected from oceanic magnetic anomalies (Ogg 2012) reveals that the lower normal (N1) zone and upper (N2) zone are respectively correlated to Chron C2r.1n, spanning 2.148–2.128 Ma, and Chron C2n, spanning 1.948–1.778 Ma. It is therefore concluded that the lava sequence of the Dobi section records a polarity sequence of Chrons C2r.2r–C2r.1n–C2r.1r–C2n.

Table 3. Summarized results of successful palaeointensity experiments of the Tsunakawa–Shaw method for specimens.

Flow name	Specimen name	TM curve	NRM ₀ (10 ⁻⁵ Am ² kg ⁻¹)	ARM ₀ (10 ⁻⁵ Am ² kg ⁻¹)	LTD (%)	First heating				Second heating							
						ΔH ₁ (mT)	Slope _{A1}	Slope _N	f _N	r _N	ΔH ₂ (mT)	Slope _{A2}	Slope _T	f _T	r _T	F _L (μT)	F (μT)
DB18 (N/N ₀ = 2/2)																	
	DB18-1-1-LA4	S	505	184	22.7	18–90	0.875	1.84 ± 0.04	0.501	0.995	14–180	1.01	1.04 ± 0.01	0.773	0.999	25.0	46.0 ± 1.0
	DB18-2-B-1	S	243	172	23.5	10–180	0.703	0.389 ± 0.005	0.784	0.997	26–180	1.18	1.05 ± 0.01	0.683	0.998	50.0	19.5 ± 0.3
DB17 (N/N ₀ = 2/3)																	
	DB17-1-3-D	S	268	218	25.0	16–180	0.541	0.599 ± 0.009	0.534	0.996	6–180	0.879	0.986 ± 0.009	0.844	0.998	20.0	12.0 ± 0.2
	DB17-2-3-C	S	256	159	27.0	0–180	0.944	0.893 ± 0.013	0.964	0.996	18–180	0.979	1.02 ± 0.01	0.809	0.999	25.0	22.3 ± 0.3
DB16 (N/N ₀ = 4/4)																	
	DB16-1-2-A	S	89.5	43.6	38.7	0–150	0.922	0.977 ± 0.017	0.960	0.995	0–180	0.987	1.04 ± 0.01	0.960	0.998	25.0	24.4 ± 0.4
	DB16-2-A	S	46.8	47.5	28.8	18–90	0.857	0.801 ± 0.017	0.587	0.996	0–180	0.978	1.04 ± 0.01	1.01	0.999	25.0	20.0 ± 0.4
	DB16-3-2-LA	S	51.6	56.3	30.7	14–110	0.868	0.731 ± 0.015	0.720	0.995	0–180	1.02	1.03 ± 0.01	1.01	0.998	25.0	18.3 ± 0.4
	DB16-4-B	S	58.5	28.2	51.3	20–110	0.939	0.935 ± 0.021	0.488	0.995	16–180	0.963	1.05 ± 0.01	0.704	0.998	25.0	23.4 ± 0.5
DB15 (N/N ₀ = 4/7)																	
	*DB15-1-B	S	106	119	29.6	15–80	1.32	0.383 ± 0.011	0.692	0.996	0–140	1.02	0.985 ± 0.002	0.996	1.00	25.0	9.56 ± 0.28
	DB15-1-3-B	S	99.5	117	27.5	12–90	1.18	0.522 ± 0.011	0.800	0.995	0–180	1.01	1.01 ± 0.01	0.993	0.999	20.0	10.4 ± 0.2
	DB15-2-2-A	S	118	93.1	30.9	16–120	0.569	0.664 ± 0.013	0.567	0.995	12–180	1.03	1.04 ± 0.02	1.09	0.996	25.0	16.6 ± 0.3
	DB15-3-B-1	S	93.9	79.7	30.6	4–150	1.26	0.482 ± 0.009	0.982	0.995	4–180	1.05	0.990 ± 0.006	0.974	0.999	25.0	12.1 ± 0.2
DB14 (N/N ₀ = 4/4)																	
	DB14-1-3-A2	S	217	121	20.6	0–160	0.910	0.723 ± 0.013	0.950	0.995	0–180	0.990	1.01 ± 0.01	1.01	1.00	25.0	18.1 ± 0.3
	DB14-2-C-A	S	178	95.2	27.3	0–180	0.933	0.724 ± 0.009	0.973	0.997	6–180	1.02	0.976 ± 0.006	0.955	0.999	25.0	18.1 ± 0.2
	DB14-3-1-B1	S	197	106	25.0	12–160	0.855	0.743 ± 0.013	0.861	0.995	0–180	0.990	1.01 ± 0.01	1.01	0.999	25.0	18.6 ± 0.3
	DB14-4-B	S	319	164	20.1	0–150	1.04	0.768 ± 0.014	0.948	0.995	0–180	0.981	1.03 ± 0.01	1.01	1.00	25.0	19.2 ± 0.4
DB13 (N/N ₀ = 4/4)																	
	DB13-1-C	S	93.8	69.1	30.8	24–180	0.910	0.447 ± 0.008	0.774	0.996	0–180	0.965	0.975 ± 0.006	1.01	0.999	25.0	11.2 ± 0.2
	DB13-2-1-U1	S	92.3	69.6	28.8	20–170	0.878	0.432 ± 0.008	0.863	0.995	0–180	0.973	0.981 ± 0.009	0.986	0.999	25.0	10.8 ± 0.2
	DB13-3-1-A	S	98.0	68.1	27.5	22–180	1.04	0.538 ± 0.010	0.785	0.996	0–180	0.919	1.031 ± 0.01	1.02	0.999	25.0	13.5 ± 0.3
	DB13-4-2-B	S	119	90.8	34.2	26–140	0.906	0.377 ± 0.009	0.717	0.995	0–180	0.979	1.02 ± 0.01	1.00	1.00	25.0	9.43 ± 0.23
DB12 (N/N ₀ = 4/4)																	
	DB12-1-5-B1	S	293	113	42.9	0–180	0.895	0.921 ± 0.013	0.991	0.996	0–180	0.977	1.033 ± 0.01	1.01	0.999	25.0	23.0 ± 0.3
	DB12-2-2-U1	S	247	119	38.0	0–170	0.951	0.839 ± 0.014	0.949	0.995	0–180	1.02	0.986 ± 0.004	1.00	1.00	25.0	21.0 ± 0.4
	DB12-3-3-B	S	206	52.4	38.5	2–180	0.866	1.81 ± 0.02	0.958	0.997	26–180	0.997	0.975 ± 0.009	0.658	0.999	25.0	45.1 ± 0.5
	DB12-4-5-A	S	171	37.1	27.5	0–180	0.918	1.69 ± 0.01	0.983	0.999	0–180	0.974	0.970 ± 0.007	0.985	0.999	25.0	42.3 ± 0.3
DB10 (N/N ₀ = 0/4)																	
DB9A2 (N/N ₀ = 3/3)																	
	DB9-5-2-U	S-	84.8	273	7.0	16–180	1.21	0.336 ± 0.005	0.896	0.996	0–180	1.06	0.963 ± 0.007	1.00	0.999	10.0	3.36 ± 0.05
	DB9-5-2-L	S-	77.7	271	6.7	16–180	1.20	0.673 ± 0.013	0.883	0.995	0–180	1.07	0.984 ± 0.009	0.990	0.998	5.00	3.37 ± 0.07
	DB9-8-1-L	S	19.3	162	18.8	26–180	0.485	0.417 ± 0.009	0.506	0.995	0–180	1.03	0.988 ± 0.015	0.981	0.996	10.0	4.17 ± 0.09

Table 3 – *continued.*

Flow name	Specimen name	TM curve	NRM ₀ (10 ⁻⁵ Am ² kg ⁻¹)	ARM ₀ (10 ⁻⁵ Am ² kg ⁻¹)	LTD (%)	First heating				Second heating					F _L (μT)	F (μT)	
						ΔH ₁ (mT)	Slope _{A1}	Slope _N	f _N	r _N	ΔH ₂ (mT)	Slope _{A2}	Slope _T	f _T			r _T
DB9A1 (N/N ₀ = 1/4)																	
	DB9-6-3-C	S	95.0	154	20.0	8–85	1.36	1.15 ± 0.02	0.797	0.995	0–180	0.994	1.02 ± 0.01	1.00	0.999	5.00	5.74 ± 0.10
DB9B (N/N ₀ = 3/7)																	
	DB9-3-2-U2	M-	222	110	24.3	10–140	0.557	1.88 ± 0.04	0.661	0.995	12–180	1.02	1.03 ± 0.01	0.823	0.997	10.0	18.8 ± 0.4
	DB9-4-B	S	102	92.3	33.6	45–160	0.554	0.657 ± 0.015	0.321	0.995	0–180	0.992	0.993 ± 0.006	0.982	0.999	25.0	16.4 ± 0.4
	DB9-4-C-1	S	99.8	94.0	31.8	40–160	0.529	0.877 ± 0.022	0.322	0.995	0–180	0.993	0.998 ± 0.010	0.993	0.998	20.0	17.5 ± 0.4
DB8 (N/N ₀ = 2/4)																	
	DB8-2-1	S	134	132	24.3	20–100	0.600	0.337 ± 0.008	0.459	0.995	0–180	0.809	0.952 ± 0.016	0.898	0.995	15.0	5.06 ± 0.12
	DB8-4-3-B	S	130	125	24.6	14–180	0.568	0.517 ± 0.005	0.716	0.998	0–180	0.975	0.980 ± 0.008	0.984	0.999	25.0	12.9 ± 0.1
DB7 (N/N ₀ = 4/4)																	
	DB7-1-B	S	201	90.0	36.3	12–120	0.818	0.872 ± 0.017	0.761	0.995	0–180	0.984	0.997 ± 0.003	1.00	1.00	25.0	21.8 ± 0.4
	DB7-2-3-B	S	145	76.8	36.3	8–180	0.793	0.867 ± 0.013	0.928	0.996	0–180	0.991	0.989 ± 0.008	0.981	0.999	25.0	21.7 ± 0.3
	DB7-3-1-B4	S	212	118	27.5	12–130	0.802	0.885 ± 0.017	0.773	0.995	0–180	0.976	1.01 ± 0.00	0.997	1.00	25.0	22.1 ± 0.4
	DB7-4-2-A3	S	230	206	9.9	0–180	0.990	0.670 ± 0.007	0.972	0.998	0–180	1.01	0.995 ± 0.003	0.995	1.00	25.0	16.8 ± 0.2
DB6 (N/N ₀ = 1/5)																	
	DB6-3-A	S	78.5	95.9	28.6	18–80	0.665	0.334 ± 0.009	0.445	0.995	0–180	0.974	1.03 ± 0.00	0.996	1.00	25.0	8.35 ± 0.23
DB5 (N/N ₀ = 0/3)																	
DB4 (N/N ₀ = 4/5)																	
	DB4-1-B	M-	42.7	81.9	29.7	16–180	0.318	0.301 ± 0.005	0.475	0.996	0–180	0.966	0.994 ± 0.004	1.00	1.00	25.0	7.53 ± 0.05
	DB4-1-C	M-	30.3	85.3	27.7	12–80	0.343	0.717 ± 0.017	0.430	0.995	0–180	1.02	0.985 ± 0.011	1.00	0.998	10.0	7.17 ± 0.17
	DB4-2-2-M	M-	32.0	105	32.6	14–90	0.402	0.769 ± 0.018	0.533	0.995	10–180	1.02	0.952 ± 0.013	0.905	0.997	10.0	7.69 ± 0.18
	DB4-4-A	M-	33.3	116	29.9	10–180	0.532	0.803 ± 0.013	0.762	0.995	0–180	1.03	1.01 ± 0.02	0.982	0.996	10.0	8.03 ± 0.13
DB3 (N/N ₀ = 3/5)																	
	DB3-2-1-L	S-	30.5	219	7.3	26–180	1.49	0.477 ± 0.010	0.614	0.995	0–180	1.09	0.996 ± 0.010	1.01	0.998	10.0	4.77 ± 0.10
	DB3-3-2-L	S-	83.5	217	8.3	10–180	1.30	1.28 ± 0.02	0.915	0.996	0–180	1.05	0.993 ± 0.013	0.987	0.997	5.00	6.39 ± 0.10
	DB3-4-3-B	S-	44	122	16.0	26–110	1.53	0.461 ± 0.012	0.551	0.995	0–180	0.996	0.973 ± 0.006	1.01	0.999	10.0	4.61 ± 0.12
DB2 (N/N ₀ = 6/6)																	
	*DB2-1-B	S	415	146	38.8	30–80	0.801	1.19 ± 0.04	0.313	0.996	10–140	0.961	1.05 ± 0.01	0.856	1.00	25.0	29.8 ± 1.0
	DB2-1-C-1	S	388	149	32.3	8–120	0.866	1.15 ± 0.02	0.855	0.995	0–180	0.981	1.05 ± 0.01	0.991	1.00	25.0	28.8 ± 0.5
	*DB2-2-B	S	404	191	21.6	20–90	0.816	1.12 ± 0.04	0.468	0.995	0–140	1.01	0.954 ± 0.009	0.976	0.999	25.0	28.0 ± 1.0
	DB2-2-C	S	367	185	18.8	12–110	0.817	1.06 ± 0.02	0.698	0.995	0–180	0.968	0.998 ± 0.004	0.999	1.00	25.0	26.6 ± 0.5
	DB2-3-B	S	346	162	27.8	12–80	0.735	1.06 ± 0.02	0.629	0.995	4–180	0.965	1.05 ± 0.01	1.02	0.999	25.0	26.6 ± 0.5
	DB2-4-B	S	198	147	21.8	16–100	0.815	0.857 ± 0.018	0.556	0.995	0–180	1.01	0.953 ± 0.006	1.02	0.999	25.0	21.4 ± 0.5

Table 3 – continued.

Flow name	Specimen name	TM curve	NRM ₀ (10 ⁻⁵ Am ² kg ⁻¹)	ARM0 ₀ (10 ⁻⁵ Am ² kg ⁻¹)	LTD (%)	First heating				Second heating				<i>r</i> _T	<i>F</i> _L (μT)	<i>F</i> (μT)	
						Δ <i>H</i> ₁ (mT)	Slope _{A1}	Slope _N	<i>f</i> _N	<i>r</i> _N	Δ <i>H</i> ₂ (mT)	Slope _{A2}	Slope _T				<i>f</i> _T
DB1 (<i>N/N</i> ₀ = 4/4)																	
	DB1-1-B	M-	95.7	105	21.7	20–85	0.633	0.935 ± 0.024	0.317	0.995	0–180	1.05	0.979 ± 0.005	0.996	0.999	20.0	18.7 ± 0.5
	DB1-3-1-M	S	131	107	23.3	14–80	0.730	1.09 ± 0.02	0.388	0.996	0–180	1.03	1.00 ± 0.00	0.996	1.00	20.0	21.9 ± 0.4
	DB1-3-2-U	S	260	103	20.8	18–110	0.635	0.777 ± 0.017	0.369	0.995	0–180	1.09	0.995 ± 0.005	0.992	1.00	25.0	19.4 ± 0.4
	DB1-3-2-M	S	147	97.3	18.9	18–80	0.605	0.787 ± 0.019	0.310	0.995	0–180	1.07	1.04 ± 0.01	0.987	0.999	20.0	15.7 ± 0.4
DB0 (<i>N/N</i> ₀ = 0/2)																	
DB(-1)A (<i>N/N</i> ₀ = 1/4)																	
	DB(-1)-6-B	S	169	104	30.6	22–85	0.661	0.554 ± 0.015	0.545	0.995	0–180	1.01	1.03 ± 0.01	0.994	0.999	25.0	13.9 ± 0.4
DB(-1)B (<i>N/N</i> ₀ = 3/3)																	
	DB(-1)-1-B	M-	158	148	26.6	14–85	0.303	1.08 ± 0.02	0.328	0.995	0–180	0.965	0.960 ± 0.008	0.997	0.999	25.0	26.9 ± 0.5
	DB(-1)-3-1-L13	S	349	128	24.9	12–100	0.904	1.80 ± 0.04	0.624	0.995	0–180	0.973	0.950 ± 0.009	0.987	0.998	25.0	45.1 ± 1.0
	DB(-1)-4-1-L	M-	257	176	28.0	12–150	0.379	0.879 ± 0.017	0.516	0.995	0–180	0.992	1.01 ± 0.01	1.00	0.999	25.0	22.0 ± 0.4
DB(-2) (<i>N/N</i> ₀ = 1/1)																	
	DB(-2)-3-A	M-	321	167	20.9	22–85	0.623	1.05 ± 0.03	0.438	0.995	0–180	0.991	1.02 ± 0.01	1.00	0.999	25.0	26.2 ± 0.8
DB(-3) (<i>N/N</i> ₀ = 2/2)																	
	DB(-3)-1-1-U	M-	105	91.6	19.4	8–180	0.700	0.636 ± 0.010	0.904	0.996	0–180	0.999	1.04 ± 0.01	0.998	1.00	25.0	15.9 ± 0.3
	DB(-3)-4-A	M-	108	77.3	24.6	18–80	0.522	0.948 ± 0.011	0.420	0.999	10–180	1.06	1.04 ± 0.01	0.867	0.999	25.0	23.7 ± 0.3
DB(-4) (<i>N/N</i> ₀ = 2/4)																	
	DB(-4)-2-1-U	M-	219	130	16.4	24–80	1.03	0.874 ± 0.024	0.509	0.995	0–180	1.02	1.02 ± 0.00	1.01	1.00	20.0	17.5 ± 0.5
	DB(-4)-4-3-D	M-	253	135	15.4	45–130	1.59	1.09 ± 0.03	0.413	0.996	0–180	1.03	0.986 ± 0.007	1.01	0.999	25.0	27.4 ± 0.8
DB(-5) (<i>N/N</i> ₀ = 3/3)																	
	DB(-5)-1-3-B	S-	219	171	8.8	26–100	0.940	1.01 ± 0.03	0.579	0.995	0–180	1.03	1.03 ± 0.01	1.01	0.999	10.0	10.1 ± 0.3
	DB(-5)-2-1-U	S	209	162	11.9	45–120	1.17	0.565 ± 0.015	0.496	0.995	0–180	1.00	0.988 ± 0.004	0.995	1.00	25.0	14.1 ± 0.4
	DB(-5)-3-3-B	S	378	264	7.7	16–180	0.989	0.484 ± 0.009	0.985	0.995	0–180	1.17	1.05 ± 0.01	0.989	1.00	25.0	12.1 ± 0.2
DB(-6) (<i>N/N</i> ₀ = 3/4)																	
	DB(-6)-2-B	M-	369	176	12.7	14–180	0.702	1.11 ± 0.01	0.733	0.998	0–180	1.02	1.02 ± 0.01	1.01	1.00	25.0	27.6 ± 0.3
	DB(-6)-2-1-U	M-	601	195	14.8	24–180	0.750	1.88 ± 0.04	0.503	0.995	0–180	1.01	1.02 ± 0.01	1.00	0.997	25.0	47.0 ± 1.0
	DB(-6)-3-3-A	M-	741	236	8.9	14–95	0.266	1.04 ± 0.02	0.362	0.995	0–180	0.974	1.03 ± 0.01	0.991	0.999	25.0	25.9 ± 0.5
DB(-7) (<i>N/N</i> ₀ = 0/1)																	

Column headings: Flow name, parentheses with '*N/N*₀' indicate the number of successful results per flow/the number of specimens subjected to the Tsunakawa–Shaw method; Specimen name, the individual specimen subjected to the palaeointensity experiment; TM curve, type of corresponding thermomagnetic curve; NRM₀ & ARM0, NRM and ARM0 intensities after LTD (10⁻⁵ Am² kg⁻¹); LTD (%), ratio of the component demagnetized by LTD to the initial NRM before LTD; Δ*H*₁ & Δ*H*₂, intervals of AF steps chosen for the slope calculation as a linear segment in the NRM–TRM1* and TRM1–TRM2* diagrams, respectively; Slope_{A1} & Slope_{A2}, slopes for the Δ*H*₁ in the ARM0–ARM1 diagram and Δ*H*₂ in the TRM1–TRM2* diagram, respectively; Slope_N & Slope_T, slopes determined for the Δ*H*₁ in the NRM–TRM1* diagram and Δ*H*₂ in the TRM1–TRM2* diagram, respectively; *f_N* & *f_T*, NRM and TRM1 fractions of the linear segments in the NRM–TRM1* and TRM1–TRM2* diagrams; *r_N* & *r_T*, correlation coefficients of pairs of data for the interval in the NRM–TRM1* and TRM1–TRM2* diagrams; *F_L* (μT), laboratory-induced DC field for imparting TRM1 and TRM2; *F* (μT), palaeointensity estimate calculated from the Slope_N and its experimental error. In the column of Specimen name, * denotes specimen for which the spinner magnetometer (Natsuhara Giken SMM-85) and the AF demagnetizer (DEM-8601C, Natsuhara Giken) were used. For the others, the DSPIN-2 system is used.

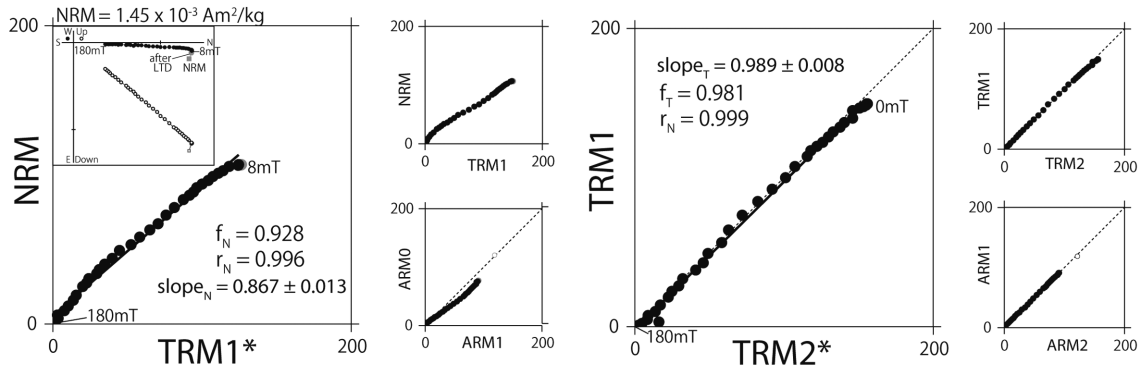
Table 4. Summarized results of successful palaeointensity experiments of the IZZ1–Thellier method for specimens.

Flow name	Specimen name	TM curve	NRM ₀ (10 ⁻⁵ Am ² kg ⁻¹)	n	ΔT (°C)	r	f	q	MAD _{Anc} (°)	θ _{DANG} (°)	dev (%)	n _{pTRM}	DRAT (%)	CDRAT (%)	Slope	F _L (μT)	F (μT)
DB18 (N/N ₀ = 1/2)	DB18-1-1-U	S	687	10	400–580	0.994	0.757	17.3	1.5	2.2	2.4	4	5.7	6.1	1.71 ± 0.07	25.0	42.8 ± 1.8
DB17 (N/N ₀ = 0/2)																	
DB16 (N/N ₀ = 0/3)																	
DB15 (N/N ₀ = 1/4)																	
DB14 (N/N ₀ = 2/4)	DB15-4-A	S	482	8	460–580	0.993	0.741	12.4	2.4	3.7	3.9	3	4.5	3.9	1.14 ± 0.06	25.0	28.5 ± 1.5
DB14-1-3-A2		S	236	8	490–600	0.996	0.796	17.6	3.8	5.0	4.1	4	–4.4	0.6	0.646 ± 0.025	25.0	16.2 ± 0.6
DB14-4-A		S	357	9	450–600	0.999	0.902	38.3	1.2	0.7	0.6	3	–1.3	0.9	0.816 ± 0.015	25.0	20.4 ± 0.4
DB13 (N/N ₀ = 0/4)																	
DB12 (N/N ₀ = 2/3)																	
DB12-3-3-A		S	205	13	300–600	0.997	0.881	35.2	1.5	2.7	2.7	6	2.9	5.3	1.98 ± 0.04	25.0	49.5 ± 1.0
DB12-4-5-B		S	180	9	460–600	0.996	0.666	16.2	1.8	3.4	2.3	4	4.2	6.8	2.10 ± 0.07	25.0	52.5 ± 1.9
DB11 (N/N ₀ = 0/1)																	
DB10 (N/N ₀ = 0/1)																	
DB9A2 (N/N ₀ = 0/1)																	
DB9A1 (N/N ₀ = 0/2)																	
DB9B (N/N ₀ = 0/4)																	
DB8 (N/N ₀ = 0/2)																	
DB7 (N/N ₀ = 3/4)																	
DB7-1-A		S	209	12	360–620	0.996	0.915	28.2	1.5	1.2	1.1	5	–2.5	–3.1	1.02 ± 0.03	25.0	25.5 ± 0.8
DB7-2-3-A		S	129	14	200–600	0.994	0.881	26.1	2.5	4.1	4.3	7	4.4	3.4	0.893 ± 0.028	25.0	22.3 ± 0.7
DB7-4-2-A2		S	268	11	350–580	0.991	0.706	14.1	2.7	4.0	4.0	4	6.6	–1.5	0.761 ± 0.034	25.0	19.0 ± 0.9
DB6 (N/N ₀ = 0/4)																	
DB4 (N/N ₀ = 0/1)																	
DB3 (N/N ₀ = 0/3)																	
DB2 (N/N ₀ = 3/4)																	
DB2-1-A		S	478	9	400–600	0.991	0.824	13.6	1.9	2.8	2.7	4	2.1	2.3	1.41 ± 0.07	25.0	35.3 ± 1.8
DB2-2-A		S	537	11	400–620	0.990	0.922	17.3	1.0	0.7	0.6	5	–1.0	0.3	1.10 ± 0.05	25.0	27.5 ± 1.3
DB2-3-A		S	397	8	500–620	0.990	0.703	10.2	1.4	0.8	0.6	3	0.9	0.0	0.994 ± 0.057	25.0	24.9 ± 1.4
DB1 (N/N ₀ = 0/1)																	
DB0 (N/N ₀ = 0/1)																	
DB(-1)A (N/N ₀ = 0/3)																	
DB(-1)B (N/N ₀ = 0/1)																	

Column headings: Flow name, parentheses with 'N/N₀' indicate the number of successful results per flow/the number of specimens subjected; Specimen name, the individual specimen subjected; TM curve, corresponding type of thermomagnetic curve; NRM, initial NRM intensity; n, ΔT, |r|, f, and g, number of the data points, temperature interval in °C, correlation coefficient, NRM fraction, and quality factor on the Arai plot to estimate the best-fit linear segment and the palaeointensity, respectively (Coe *et al.* 1978); MAD_{Anc} (°), MAD of the anchored directional fit on the vector component diagram; θ_{DANG} (°), difference angle between the free-floating best-fit direction and direction between data centre of mass and the origin of the vector component diagram (Tanaka & Kobayashi 2003); dev (°), intensity deviation of the free-floating principal component from the origin, normalized by the initial NRM intensity (Tanaka & Kobayashi 2003); n_{pTRM}, number of pTRM checks in the interval; DRAT (%), maximum difference produced by a pTRM check, normalized by the length of the best-fit line, for the interval (Selkin & Tauxe 2000; CDRAT (%), cumulative DRAT as the sum of the signed pTRM differences for the interval (Kissel & Laj 2004); Slope, slope of the linear NRM–TRM portion and its standard error; F_L (μT), laboratory-induced DC field for TRM; F (μT), calculated palaeointensity.

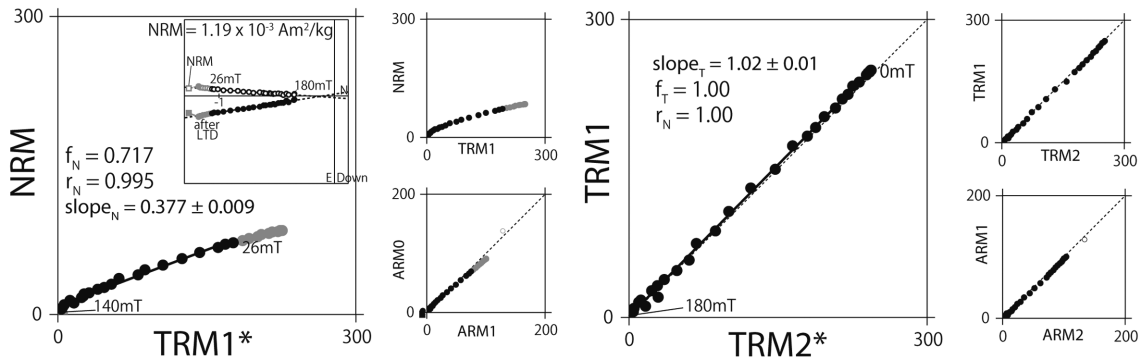
(a) DB7-2-3-B (Flow DB7)

$F = 21.7 \mu\text{T}$ ($F_L = 25.0 \mu\text{T}$)



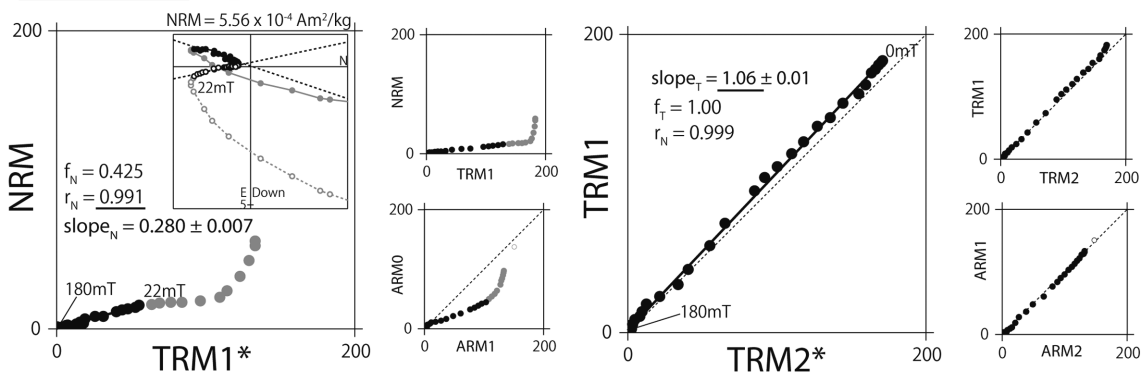
(b) DB13-4-2-B (Flow DB13)

$F = 9.43 \mu\text{T}$ ($F_L = 25.0 \mu\text{T}$)



(c) DB4-3-A (Flow DB4)

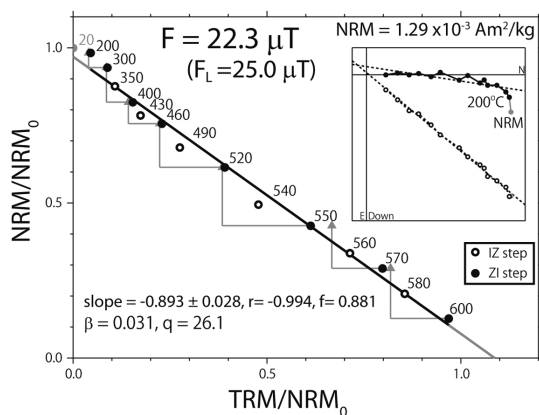
rejected ($F_L = 25.0 \mu\text{T}$)



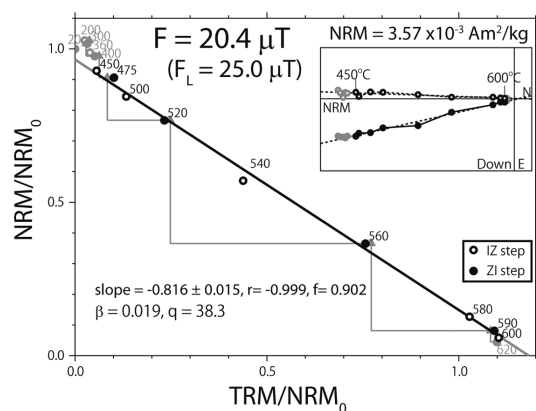
Unit: $10^{-5} \text{ Am}^2/\text{kg}$

Figure 8. Representative palaeointensity results obtained by using the Tsunakawa–Shaw method. (a, b) Examples of successful results for specimens DB7-2-3-B from flow DB7 and DB13-4-2-B from flow DB13, respectively. F (μT) is the evaluated palaeointensity. (c) An example of an unsuccessful result for specimen DB 4-3-A from flow DB4. Diagrams for NRM–TRM1*, NRM–TRM1 and ARM0–ARM1 illustrate results from the first laboratory heating; those for TRM1–TRM2*, TRM1–TRM2 and ARM1–ARM2 are from the second heating. Linear portions consist of black solid symbols for each diagram, which are used for slope calculations. Orthogonal vector component plots for the low-temperature demagnetization (LTD)–alternating field demagnetization (AFD) results of NRMs are also shown as insets in the NRM–TRM1* diagrams.

(a) DB7-2-3-A (Flow DB7)



(b) DB14-4-A (Flow DB14)



(c) DB16-3-2-U (Flow DB16)

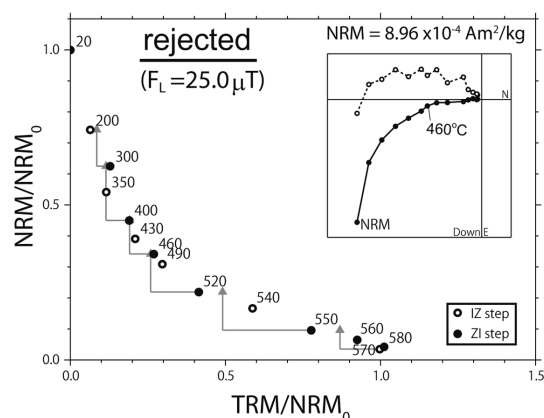


Figure 9. Representative palaeointensity results obtained by using the IZZI–Thellier method with partial thermoremanent magnetization (pTRM) checks. (a, b) Representative successful results for DB7-2-3-A and DB13-4-2-A. Black circles indicate data points used for palaeointensity calculations and grey symbols indicate those that have been omitted. (c) Example of unsuccessful result for DB16-3-2-U. ZI steps are indicated by closed circles, whereas IZ steps are shown by open circles. Triangle symbols indicate pTRM checks. F (μT) is a palaeointensity estimate. Orthogonal vector projection plots of the remanences in the zero-field steps are also shown as insets in the Arai diagrams.

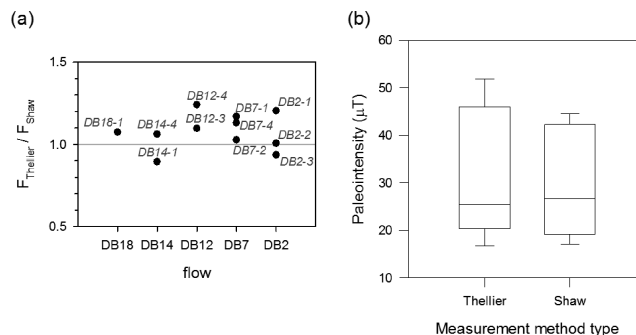


Figure 10. Comparisons of palaeointensities obtained from the Tsunakawa–Shaw method and the IZZI–Thellier method for 11 pairs of results. (a) Plot of ratio of the Thellier palaeointensity to the Tsunakawa–Shaw palaeointensity versus flow. Labels denote the sample code number for each block sample. (b) Box plot of palaeointensity determined versus type of palaeointensity measurement methods. The ends of the boxes define the 25th and 75th percentiles, with a line at the median and error bars defining the 10th and 90th percentiles.

The lava flows of the Dobi section record the palaeomagnetic field of the normal Chron of C2r.1n, commonly referred to as the Réunion Subchron (e.g. Channell *et al.* 2003). Because the ages of the base and top of the Réunion Subchron were dated at 2.153 and 2.115 Ma, respectively, from a deep-sea sediment core of ODP site 981 (Channell *et al.* 2003), our mean K–Ar age of 2.18 ± 0.06 Ma from the lower normal chron (N1) cannot be distinguished from that of the Réunion Subchron with the uncertainty.

Our present data indicate that the Réunion Subchron is a single full normal polarity chron and is not consistent with two Réunion events hypothesis (e.g. Gromme & Hay 1971; Carlut *et al.* 1999; Kidane *et al.* 1999; Kidane *et al.* 2007). A single normal polarity chron for the Réunion Subchron was determined from a number of continuous palaeomagnetic records of piston cores from the equatorial Pacific (EPAPIA-3 Ma, Yamazaki & Oda 2005), ODP 981 cores with an unusually high sedimentation rate from the North Atlantic (Channell *et al.* 2003) and IODP Site U1314 in the North Atlantic (Ohno *et al.* 2012).

Since two Réunion events were proposed by Gromme & Hay (1971), little evidence for two events within a single stratigraphic section has been noted. In particular, in the single volcanic section, two possible Réunion Subchrons have been reported from only the Gamarrí volcanic section in the Afar area (Carlut *et al.* 1999; Kidane *et al.* 1999). However, only the younger Réunion Subchron was recorded as the normal polarity zone; the older Réunion Subchron revealed only anomalous inclinations. In the Chinese loess sections, two normal polarity intervals have been reported (Rolph *et al.* 1989; Zheng *et al.* 1992). However, they do not represent strong evidence for two events because of the difficulty in interpreting magnetostratigraphies below the Olduvai and acquiring pDRM as a remanence. The fluvio-lacustrine deposits of the Plio–Pleistocene Shungura Formation in Southwest Ethiopia yielded two complete normal polarity intervals (Kidane *et al.* 2007), in which the younger subchron was recorded by one palaeomagnetic datum and had a short duration of ~ 18 kyr. Therefore, it is suggested that one of two events, if it exists, is likely a very brief normal polarity period or a geomagnetic excursion.

We estimated an average extrusion rate assuming that the ages of flows DB6 and DB17 correspond to those at bases of Chron C2r.1n (2.148 Ma) and Chron C2n (1.945 Ma) according to GPTS2012. An average extrusion rate of the lava sequence corresponds to an average interval of 15.6 kyr between flows. Therefore, the lava

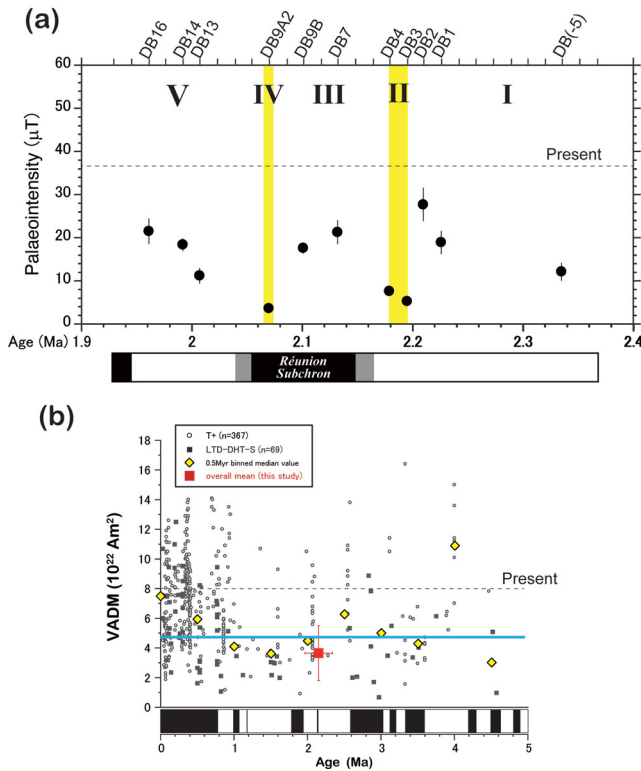


Figure 11. (a) Palaeointensity variations in the lower Matuyama Chron obtained from the present study. Ages are estimated as a linear function of frequency of lava extrusions. Circles indicate combined palaeointensity data from both the Tsunakawa–Shaw and the IZZI–Thellier data, meeting the flow-mean acceptance criteria ($N_F \geq 3$ and $\sigma_F \leq 20$ per cent). Low-palaeointensity intervals are indicated in yellow. The dashed line represents the present-day field intensity. The associated magnetic polarity stratigraphy interpreted in this study (Fig. 2) is also shown. (b) Comparison of palaeointensity in virtual axial dipole moment (VADM) obtained in this study (red squares), with data selected during the past 5 Myr from the International Association of Geomagnetism and Aeronomy (IAGA) palaeointensity database (Biggin & Paterson 2014; <http://earth.liv.ac.uk/pint/>). Solid squares are the Tsunakawa–Shaw results (LTD-DHT-S). Open circles are the Thellier-type results with pTRM checks (T+). All data are from individual cooling units and meet the selection criteria ($N_F \geq 3$, $\sigma_F \leq 20$ per cent, and stable polarity). All palaeointensities were converted to VADM by using latitudes at their sampling sites. Yellow diamonds are median values calculated for 0.5 Myr bins. Blue solid line is the average value for the last 5 Myr by calculating a grand median value of all the median values (Yellow diamonds). Dashed line is the present field intensity. Geomagnetic Polarity Time Scale (GPTS2012; Ogg 2012) for reference is also shown below the abscissa axis.

sequence of the Dobi section covers a time period of 0.44 Myr spanning from 2.37 Ma to 1.93 Ma (Fig. 11a; note that the lower age bound is extrapolated based on the average extrusion rate). The present study can provide measurements of the geomagnetic field every ~ 16 kyr; therefore, it is hard to detect a possibly very brief subchron or excursion with a duration shorter than 16 kyr.

Two possible excursions are reported in the period of 1.93–2.37 Ma in the lower Matuyama Chron from ODP sites 980–984 (Laj & Channell 2009), that is, pre-Réunion I (2.236 Ma) and Pre-Olduvai excursions (1.977 Ma). However, no clear excursions are observed in our study, which suggests that these excursions are probably due to local geomagnetic effects or very short duration less than 16 kyr.

6.2 Geomagnetic field intensity in the lower Matuyama Chron

Our Tsunakawa–Shaw and IZZI–Thellier palaeointensity experiments yielded 11 reliable flow-mean palaeointensities. Fig. 11(a) shows the variations with time for the lava section based on a simple age model using the extrusion rate (an average of 15.6 kyr per flow) and the tie-point ages (2.148 and 1.945 Ma respectively; GPTS2012) of flows DB6 and DB17. This implies that our palaeointensity data span between 2.34 and 1.96 Ma. Because a previous study from the lava flow sequence at the Gamarri reported palaeointensity between 2.14 and 2.02 Ma (Carlut *et al.* 1999), our data cover the same time period and provide a chance to examine the geomagnetic behaviour in the lower Matuyama Chron. Two striking aspects in intensity variation from the observed record are noted. Firstly, two periods have an extremely low ($< 8 \mu\text{T}$) palaeointensity between 2.20 and 2.07 Ma. Secondly, the time-averaged field intensity ($15 \mu\text{T}$) through a time period of 2.34–1.96 Ma is weak as 41 per cent of the present-day field.

6.2.1 ‘W-shape’ palaeointensity variation: two intervals with low intensity around the Réunion Subchron

Palaeointensity variation of the Dobi area is characterized by five intervals which reveal a ‘W-shape’ variation of high–low–high–low–high palaeointensities between 2.34 and 1.96 Ma from the late stage of Chron C2r.2r to Chron C2r.1r. Relatively high intensity with an average of $19.6 \pm 7.8 \mu\text{T}$ occurs from an age of younger than 2.34 to 2.21 Ma (Interval I in Fig. 11a). Then, an extremely low palaeointensity with an average of $6.4 \mu\text{T}$ is observed prior to the Réunion Subchron, with an inferred duration of 16 kyr (Interval II in Fig. 11a). During the Réunion Subchron, relatively high palaeointensity with an average of $19.5 \mu\text{T}$ occurs (Interval III in Fig. 11a) then it is followed by extremely low palaeointensity ($3.6 \mu\text{T}$) at approximately 2.07 Ma (Interval IV). The palaeointensity is then rejuvenated gradually with an average of $17.0 \pm 5.3 \mu\text{T}$ during the following reverse polarity interval (Interval V in Fig. 11a). One of the most striking feature is the existence of two intervals with extremely low field intensities with an average of $5.5 \pm 2.0 \mu\text{T}$, which is equivalent to only ~ 15 per cent of the present geomagnetic field.

Carlut *et al.* (1999) reported palaeointensity results across the Réunion Subchron from Gamarri section belongs to the same lava sequence in Africa. Considering the acceptance criteria applied ($N_F \geq 3$ and $\sigma_F \leq 20$ per cent), only seven palaeointensities are considered acceptable and their values vary from 13.6 to $26.0 \mu\text{T}$, concentrating between the Réunion event (C2r.1n) and following reversed chron (C2n.1r). Although the selected Gamarri data do not recover the ‘W-shape’ palaeointensity structure observed in this study and have no significantly weak intensity lower than $8 \mu\text{T}$, mean palaeointensities during the Réunion Subchron ($20.2 \mu\text{T}$) and following reversed chron ($15.2 \mu\text{T}$) are in agreement with our results.

The ‘W-shape’ palaeointensity variation with two significant lows around the Réunion Subchron has been observed from deep-sea sediment cores of Ontong Java Plateau (OJP stack in Kok & Tauxe 1999) and the North Atlantic (IODP Site U1314, Ohno *et al.* 2012). However, the EPAPIA-3 Ma record from the West Caroline basin (Yamazaki & Oda 2005) and the ODP Leg 138 record from the equatorial Pacific Ocean (Valet & Meynadier 1993) appear to show an unclear peak of intensity between two field lows. Because the EPAPIA-3 Ma record was estimated by a stacking procedure of four cores, the actual palaeointensity variation could be skewed and

concealed by the stacking procedure. For the ODP Leg 138, the range of the Réunion Subchron is unclear because there is no directional change during this period. As a consequence, the similar geomagnetic field variation across the Réunion Subchron is obviously observed in the southwest Pacific Ocean and the North Atlantic, as well as Ethiopia, suggesting that this phenomenon would be a global characteristic of the geomagnetic field.

6.2.2 Dipole field low for the lower Matuyama Chron

A striking feature is that weak geomagnetic field intensity (3.63–26.9 μT) is prevalent during the lower Matuyama Chron, which is low relative to the present geomagnetic field. The average field intensity for the Dobi section, where palaeointensity data cover an age interval of 2.34–1.96 Ma, is $15.0 \pm 7.6 \mu\text{T}$. This value is 41 per cent of the present geomagnetic field intensity and corresponds to a virtual axial dipole moment (VADM) of $3.66 (\pm 1.85) \times 10^{22} \text{ Am}^2$, as shown by the red square in Fig. 11(b).

Goguitchaichvili *et al.* (1999) reported magnetostratigraphy and absolute palaeointensity estimates derived from Iceland during the Réunion Subchron (C2r.1n) and the preceding reversed polarity chron (C2r.2r). The original Thellier method (Thellier & Thellier 1959) was employed for the palaeointensity experiments. The individual mean VDMs during C2r.1n and C2r.2r chrons were $5.03 \times 10^{22} \text{ Am}^2$ and $6.25 \times 10^{22} \text{ Am}^2$, respectively. These values are larger than our estimate, but are still lower than the present geomagnetic field. Laj *et al.* (2000) also reported palaeointensity estimates of the original Thellier method and suggested a fairly large time-averaged VADM of $7.6 \times 10^{22} \text{ Am}^2$ around 2.15 Ma from the Koolau volcanic series in Oahu Island, Hawaii. This discrepancy in average VADM values may come from the overestimation of palaeointensity by the Thellier-type method (e.g. Yamamoto *et al.* 2003; Mochizuki *et al.* 2004; Oishi *et al.* 2005). Although the dipole field intensity during the Réunion Subchron reported in other studies of igneous rocks is likely not as low as our mean VDM, we believe that relatively low intensity characterizes the geomagnetic field nature in this time period.

We can also compare our mean VADM value during the lower Matuyama Chron with the average during the last 5 Myr. However, estimating a time-averaged value for the geomagnetic field intensity should be done with caution, because, as Tauxe *et al.* (2013) described, it depends not only on the selection criteria applied, but also on the time span over which the average is calculated. Available data for the last 5 Myr are selected from the International Association of Geomagnetism and Aeronomy palaeointensity database (<http://earth.liv.ac.uk/pint/>; Biggin & Paterson 2014) using the following criteria: (1) each data point is from the Tsunakawa–Shaw method or the Thellier-type method with pTRM checks; (2) each data point is averaged from three or more individual estimates ($N_F \geq 3$) and its standard deviation is within 20 per cent ($\sigma_F \leq 20$ per cent); and (3) its associated direction has a stable polarity. With the selected data, we calculated median values for 0.5 Myr bins and then calculated a grand median value of all the medians, which is $4.75 \times 10^{22} \text{ Am}^2$. Our estimated average value during the lower Matuyama Chron is low, only 77 per cent of the time-averaged value for the last 5 Myr value, which may have been caused by low geodynamo activity during this time.

This period of relatively low dipole field last for approximately 0.38 Myr, which is comparable to the mean period (0.248 Myr) of one polarity during the Cenozoic (Lowrie & Kent 2004). Long and low palaeointensity is observed in the OJP stack of the Ontong

Java Plateau data (Kok & Tauxe 1999), but the low-intensity period ceased at 2 Ma. ODP Leg 138 reveals that the relative intensity decreased from a maximum value at 2.5 Ma and reached the minimum at 1.8 Ma (Valet & Meynadier 1993). Our observation may reflect the process of gradual decrease of the geomagnetic field between 2.5 and 1.8 Ma.

7 CONCLUSIONS

Magnetostratigraphy with K–Ar ages indicates that a lava sequence of Dobi section in Afar depression records a succession of four magnetochrons (C2r.2r, C2r.1n, C2r.1r, C2n), and its age coverage, if we assume an average eruption rate of 15.6 kyr between flows, is estimated to be from 2.37 to 1.93 Ma. The observed Réunion Subchron (C2r.1n) is a single normal polarity and is inconsistent with the two Réunion events hypothesis. Palaeointensity results reveal that there are two extremely low field intensities (less than $8 \mu\text{T}$) around the Réunion Subchron, which are surrounded by the same field strength of approximately 17–20 μT (‘W-shape’ palaeointensity variation). The two extremely low field events are observed prior to and during the Réunion Subchron. Because the ‘W-shape’ palaeointensity variation is observed in sedimentary rocks collected from the southwestern Pacific Ocean and the North Atlantic as well in the Afar region of Ethiopia, it is likely to be a global characteristic of the geomagnetic field. A generally weak geomagnetic intensity of $15.0 \pm 7.6 \mu\text{T}$ ($3.66 \pm 1.85 \times 10^{22} \text{ Am}^2$ in VADM) is also observed throughout the studied lava sequence during 0.38 Myr from 2.34 to 1.96 Ma. Thus, the early stage of the Matuyama Chron can be characterized by a period of long and low geomagnetic field intensity.

ACKNOWLEDGEMENTS

We thank T. Yamamoto, G. Shogaki and Dr N. Ishikawa for their help during the sampling trip. The authors were indebted to Dr C. Gouzu of Hiruzen Institute for Geology and Chronology for K–Ar dating. We are also thankful to the Japanese Ministry of Education, Culture, Sports, Science and Technology ‘MEXT’ (Grant-in-aid Nos 19654068 and 22403012) and the Global COE Program for the Origin and Evolution of the Planetary Systems in MEXT. This study was partly performed under the cooperative research program of the Center for Advanced Marine Core Research (CMCR), Kochi University (13B009 and 13A010). We wish to thank Dr Greig A. Paterson and one anonymous reviewer for their careful and constructive comments and suggestion to improve the manuscript.

REFERENCES

- Beyene, A. & Abdelsalam, M.G., 2005. Tectonics of the Afar depression: a review and synthesis, *J. Afr. Earth Sci.*, **41**(1), 41–59.
- Biggin, A.J. & Paterson, G.A., 2014. A new set of qualitative reliability criteria to aid inferences on palaeomagnetic dipole moment variations through geological time, *Front. Earth Sci.*, **2**, doi:10.3389/feart.2014.00024.
- Carlut, J., Valet, J.P., Quidelleur, X., Courtillot, V., Kidane, T., Gallet, Y. & Gillot, P.Y., 1999. Palaeointensity across the Réunion event in Ethiopia, *Earth planet. Sci. Lett.*, **170**, 17–34.
- Channell, J.E.T., Laj, C. & Raymo, M.E., 2003. The Réunion Subchronozone at ODP Site 981 (Feni Drift, North Atlantic), *Earth planet. Sci. Lett.*, **215**, 1–12.
- Channell, J.E.T., Xuan, C. & Hodell, D.A., 2009. Stacking palaeointensity and oxygen isotope data for the last 1.5 Myr (PISO-1500), *Earth planet. Sci. Lett.*, **283**(1–4), 14–23.

- Coe, R.S., Gromme, S. & Mankinen, E.A., 1978. Geomagnetic palaeointensities from radiocarbon-dated lava flows on Hawaii and the question of the Pacific nondipole low, *J. geophys. Res.*, **83**, 1740–1756.
- Cogne, J.P., 2003. PaleoMac: a MacintoshTM application for treating palaeomagnetic data and making plate reconstructions, *Geochem. Geophys. Geosyst.*, **4**, 1007, doi:10.1029/2001GC000227.
- Courtillot, V., Achache, J., Landre, F., Bonhommet, N., Montigny, R. & Fraud, G., 1984. Episodic spreading and rift propagation: new palaeomagnetic and geochronologic data from the Afar nascent passive margin, *J. geophys. Res.*, **89**, 3315–3333.
- Day, R., Fuller, M.D. & Schmidt, V.A., 1977. Hysteresis properties of titanomagnetites: grain size and composition dependence, *Phys. Earth planet. Inter.*, **13**, 260–267.
- Dunlop, D., 2002. Theory and application of the Day plot (Mrs/Ms versus Hcr/Hc) 1. Theoretical curves and tests using titanomagnetite data, *J. geophys. Res.*, **107**, 2056, doi:10.1029/2001JB000486.
- Fisher, R.A., 1953. Dispersion on a sphere, *Proc. R. Soc. A*, **217**, 295–305.
- Gee, J.S. & Kent, D.V., 2009. Source of oceanic magnetic anomalies and the geomagnetic polarity timescale, in *Treatise on Geophysics*, Vol. 5, pp. 455–507, ed. Kono, M., Elsevier B.V.
- Glatzmaier, G.A. & Robert, P.H., 1995. A three-dimensional self-consistent computer simulation of a geomagnetic field reversal, *Nature*, **377**, 203–209.
- Goguitchaichvili, A.T., Prevot, M. & Camp, P., 1999. No evidence for strong fields during the R3-N3 Icelandic geomagnetic reversal, *Earth planet. Sci. Lett.*, **167**, 15–34.
- Gromme, C.S. & Hay, R.L., 1971. Geomagnetic polarity epochs: age and duration of the Olduvai normal polarity event, *Earth planet. Sci. Lett.*, **18**, 179–185.
- Halls, H.C., 1976. A Least-Squares Method to find a Remanence Direction from Converging Remagnetization Circles, *Geophys. J. Int.*, **45**, 297–304.
- Halls, H.C., 1978. The use of converging remagnetization circles in palaeomagnetism, *Phys. Earth planet. Inter.*, **16**, 1–11.
- Heider, F., Dunlop, D.J. & Soffel, H.C., 1992. Low-temperature and alternating field demagnetization of saturation remanence and thermoremanence in magnetite grains (0.037 μm to 5 mm), *J. geophys. Res.*, **97**, 9371–9381.
- International Association of Geomagnetism and Aeronomy Working Group V-MOD, 2010. International geomagnetic reference field: the eleventh generation, *Geophys. J. Int.*, **183**, 1089–1663.
- Itaya, T., Doi, M. & Ohira, T., 1996. Very low potassium analysis by flame photometry using ultra low blank chemical lines: an application of K-Ar dating to ophiolites, *Geochem. J.*, **30**, 31–39.
- Itaya, T., Nagao, K., Inoue, K., Honjou, Y., Okada, T. & Ogata, A., 1991. Argon isotope analysis by a newly developed mass spectrometric system for K-Ar dating, *Mineral. J.*, **15**, 203–221.
- Kidane, T., Carlut, J., Courtillot, V., Gallet, Y., Quidelleur, X., Gillot, P.Y. & Haile, T., 1999. Palaeomagnetic and geochronological identification of the Reunion subchron in Ethiopian Afar, *J. geophys. Res.*, **104**, 405–419.
- Kidane, T. *et al.*, 2003. New palaeomagnetic and geochronologic results from Ethiopian Afar: block rotations linked to rift overlap and propagation and determination of a 2 Ma reference pole for stable Africa, *J. geophys. Res.*, **108**, 2102, doi:10.1029/2001JB000645.
- Kidane, T., Otofujii, Y.I., Brown, F.H., Takemoto, K. & Eshete, G., 2007. Two normal palaeomagnetic polarity intervals in the lower Matuyama Chron recorded in the Shungura Formation (Omo valley, southwest Ethiopia), *Earth planet. Sci. Lett.*, **262**, 240–256.
- Kirschvink, J.L., 1980. The least-squares line and plane and the analysis of palaeomagnetic data, *Geophys. J. R. astr. Soc.*, **62**, 699–718.
- Kissel, C. & Laj, C., 2004. Improvements in procedure and palaeointensity selection criteria (PICRIT-03) for Thellier and Thellier determinations: application to Hawaiian basaltic long cores, *Phys. Earth planet. Inter.*, **147**, 155–169.
- Kodama, K.P., 2012. *Palaeomagnetism of Sedimentary Rocks: Process and Interpretation*, Wiley-Blackwell, 157 pp.
- Kok, Y.S. & Tauxe, L., 1999. A relative geomagnetic palaeointensity stack from Ontong-Java Plateau sediments for the Matuyama, *J. geophys. Res.*, **104**, 25 401–25 413.
- Lahitte, P., Gillot, P.-Y., Kidane, T. & Courtillot, V., 2003. New age constraints on the timing of volcanism in central Afar, in the presence of propagating rifts, *J. geophys. Res.*, **108**(B2), 2123, doi:10.1029/2001JB1689.
- Laj, C. & Channell, J.E.T., 2009. Geomagnetic excursions, in *Geomagnetism*, Vol. 5, pp. 373–416, ed. Kono, M., Treatise on Geophysics, Elsevier B.V.
- Laj, C., Szeremeta, N., Kissel, C. & Guillou, H., 2000. Geomagnetic intensities at Hawaii between 3.9 and 2.1 Ma: preliminary results, *Earth planet. Sci. Lett.*, **179**, 191–204.
- Laj, C., Kissel, C., Davies, C. & Gubbins, D., 2011. Geomagnetic field intensity and inclination records from Hawaii and the Réunion Island, Geomagnetic implications, *Phys. Earth planet. Inter.*, **187**, 170–187.
- Lowrie, W. & Kent, D.V., 2004. Geomagnetic polarity timescales and reversal frequency regimes, in *Timescales of the Palaeomagnetic Field*, Vol. 145, pp. 117–129, eds Channell, J.E.T., Kent, D.V., Lowrie, W. & Meert, J.G., Geophysical Monograph, AGU.
- McFadden, P.L. & McElhinny, M.W., 1990. Classification of the reversal test in palaeomagnetism, *Geophys. J. Int.*, **103**(3), 725–729.
- Mochizuki, N., Tsunakawa, H., Oishi, Y., Wakai, S., Wakabayashi, K. & Yamamoto, Y., 2004. Palaeointensity study of the Oshima 1986 lava in Japan: implications for the reliability of the Thellier and Tsunakawa-Shaw methods, *Phys. Earth planet. Inter.*, **146**, 395–416.
- Mochizuki, N., Oda, H., Ishizuka, O., Yamazaki, T. & Tsunakawa, H., 2011. Palaeointensity variation across the Matuyama-Brunhes polarity transition: observations from lavas at Punaruu Valley, Tahiti, *J. geophys. Res.*, **116**, B06103, doi:10.1029/2010JB008093.
- Nagao, K., Nishido, M., Itaya, T. & Ogata, K., 1984. K-Ar age determination, *Bull. Hiruzen Res. Inst.*, **9**, 19–38.
- Nagata, T., Arai, Y. & Momose, K., 1963. Secular variation of the geomagnetic total force during the last 5000 years, *J. geophys. Res.*, **68**, 5277–5281.
- Ogg, J.G., 2012. Geomagnetic polarity time scale, in *The Geologic Time Scale 2012*, pp. 85–113, eds Gradstein, F.M., Ogg, J.G., Schmitz, M. & Ogg, E.G., Elsevier.
- Ohno, M. *et al.*, 2012. A detailed palaeomagnetic record between 2.1 and 2.75 Ma at IODP Site U1314 in the North Atlantic: geomagnetic excursions and the Gauss–Matuyama transition, *Geochem. Geophys. Geosyst.*, **13**, Q12Z39. <http://dx.doi.org/10.1029/2012GC004080>.
- Oishi, Y., Tsunakawa, H., Mochizuki, N., Yamamoto, Y., Wakabayashi, K. & Shibuya, H., 2005. Validity of the LTD-DHT Shaw and Thellier palaeointensity methods: a case study of the Kilauea 1970 lava, *Phys. Earth planet. Inter.*, **149**, 243–257.
- Ozima, M., Ozima, M. & Akimoto, S., 1964. Low temperature characteristics of remanent magnetization of magnetite—self-reversal and recovery phenomena of remanent magnetization, *J. Geomagn. Geoelectr.*, **16**, 165–177.
- Pullaiah, G., Irving, E., Buchan, K.L. & Dunlop, D.J., 1975. Magnetization changes caused by burial and uplift, *Earth planet. Sci. Lett.*, **28**, 133–143.
- Rolph, T.C. & Shaw, J., 1985. A new method of paleofield magnitude correction for thermally altered samples and its application to Lower Carboniferous lavas, *Geophys. J. R. astr. Soc.*, **80**, 773–781.
- Rolph, T.C., Shaw, J., Derbyshire, E. & Jingtai, W., 1989. A detailed geomagnetic record from Chinese loess, *Phys. Earth planet. Inter.*, **56**, 151–164.
- Selkin, P.A. & Tauxe, L., 2000. Long-term variations in palaeointensity, *Philos. Trans. R. Soc. Lond. A*, **358**, 1065–1088.
- Steiger, R.H. & Jäger, E., 1977. Subcommission on geochronology: convention on the use of decay constants in geo- and cosmochronology, *Earth planet. Sci. Lett.*, **36**, 359–362.
- Tanaka, H. & Kobayashi, T., 2003. Palaeomagnetism of the late Quaternary Ontake Volcano, Japan: directions, intensities, and excursions, *Earth Planets Space*, **55**, 189–202.
- Tauxe, L. & Staudigel, H., 2004. Strength of the geomagnetic field in the Cretaceous Normal Superchron: new data from submarine basaltic glass of the Troodos Ophiolite, *Geochem. Geophys. Geosyst.*, **5**, Q02H06, doi:10.1029/2003GC000635.
- Tauxe, L. & Yamazaki, T., 2009. Palaeointensity, in *Geomagnetism*, Vol. 5, pp. 509–563, ed. Kono, M., Treatise on Geophysics, Elsevier.

- Tauxe, L., Gee, J.S., Steiner, M.B. & Staudigel, H., 2013. Palaeointensity results from the Jurassic: new constraints from submarine basaltic glasses of ODP Site 801C, *Geochem. Geophys. Geosyst.*, **14**, 4718–4733.
- Taylor, J.R., 1982. *An Introduction to Error Analysis*, University Science Books.
- Thellier, E. & Thellier, O., 1959. Sur l'intensité du champ magnétique terrestre dans le passé historique et géologique, *Ann. Geophys.*, **15**, 285–376.
- Tsunakawa, H. & Shaw, J., 1994. The Shaw method of palaeointensity determinations and its application to recent volcanic rocks, *Geophys. J. Int.*, **118**, 781–787.
- Valet, J., 1975. *Geologic Map of central and southern Afar (Ethiopia and F.T.A.I.)*, 1:500 000, Beicip.
- Valet, J.P. & Meynadier, L., 1993. Geomagnetic field intensity and reversals during the past four million years, *Nature*, **366**, 234–238.
- Valet, J.P., Meynadier, L. & Guyodo, Y., 2005. Geomagnetic dipole strength and reversal rate over the past two million years, *Nature*, **435**, 802–805.
- Vandamme, D., 1994. A new method to determine paleosecular variation, *Phys. Earth planet. Inter.*, **85**(1), 131–142.
- Yamamoto, Y. & Tsunakawa, H., 2005. Geomagnetic field intensity during the last 5 Myr: Tsunakawa-Shaw palaeointensities from volcanic rocks of the Society Islands, French Polynesia, *Geophys. J. Int.*, **162**, 79–114.
- Yamamoto, Y., Tsunakawa, H. & Shibuya, H., 2003. Palaeointensity study of the Hawaiian 1960 lava: implications for possible causes of erroneously high intensities, *Geophys. J. Int.*, **153**(1), 263–276.
- Yamamoto, Y., Tsunakawa, H., Shaw, J. & Kono, M., 2007. Palaeomagnetism of the Datong monogenetic volcanoes in China: palaeodirection and palaeointensity during the middle to early Brunhes Chron, *Earth Planets Space*, **59**, 727–746.
- Yamamoto, Y., Shibuya, H., Tanaka, H. & Hoshizumi, H., 2010. Geomagnetic palaeointensity deduced for the last 300 kyr from Unzen Volcano, Japan, and the dipolar nature of the Iceland Basin excursion, *Earth planet. Sci. Lett.*, **293**, 236–249.
- Yamazaki, T. & Oda, H., 2005. A geomagnetic palaeointensity stack between 0.8 and 3.0 Ma from equatorial Pacific sediment cores, *Geochem. Geophys. Geosyst.*, **6**, Q11H20, doi:10.1029/2005GC001001.
- Zheng, H., An, Z. & Shaw, J., 1992. New contributions to Chinese Plio-Pleistocene magnetostratigraphy, *Phys. Earth planet. Inter.*, **70**, 146–153.
- Zijderveld, J.D.A., 1967. A. C. demagnetization of rocks: analysis of results, in *Methods in Palaeomagnetism*, pp. 254–286, eds Collinson, D.W., Creer, K.M. & Runcorn, S.K., Elsevier.